Chen et al. *Zool. Res.* 2022, 43(4): 615−633
https://doi.org/10.24272/j.issn.2095-8137.2022.121

ZR | Zoological Research

Article Open Access

Differences in action potential propagation speed and axon initial segment plasticity between neurons from Sprague-Dawley rats and C57BL/6 mice

Zhi-Ya Chen[1], Luxin Peng[2], Mengdi Zhao[3,7], Yu Li[1], Mochizuki Takahiko[1], Louis Tao[3,4,*], Peng Zou[2,5,6,8,*], Yan Zhang[1,*]

[1] *State Key Laboratory of Membrane Biology*, *College of Life Sciences*, *Peking University*, *Beijing* 100871, *China*
[2] *College of Chemistry and Molecular Engineering*, *Synthetic and Functional Biomolecules Center*, *Beijing National Laboratory for Molecular Sciences*, *Key Laboratory of Bioorganic Chemistry and Molecular Engineering of Ministry of Education*, *Peking University*, *Beijing* 100871, *China*
[3] *Center for Quantitative Biology*, *Academy for Advanced Interdisciplinary Studies*, *Peking University*, *Beijing* 100871, *China*
[4] *Center for Bioinformatics*, *National Laboratory of Protein Engineering and Plant Genetic Engineering*, *School of Life Sciences*, *Peking University*, *Beijing* 100871, *China*
[5] *Peking-Tsinghua Center for Life Sciences*, *Peking University*, *Beijing* 100871, *China*
[6] *PKU-IDG/McGovern Institute for Brain Research*, *Peking University*, *Beijing* 100871, *China*
[7] *Beijing Academy of Artificial Intelligence*, *Beijing* 100084, *China*
[8] *Chinese Institute for Brain Research (CIBR)*, *Beijing* 102206, *China*

ABSTRACT

Action potentials (APs) in neurons are generated at the axon initial segment (AIS). AP dynamics, including initiation and propagation, are intimately associated with neuronal excitability and neurotransmitter release kinetics. Most learning and memory studies at the single-neuron level have relied on the use of animal models, most notably rodents. Here, we studied AP initiation and propagation in cultured hippocampal neurons from Sprague-Dawley (SD) rats and C57BL/6 (C57) mice with genetically encoded voltage indicator (GEVI)-based voltage imaging. Our data showed that APs traveled bidirectionally in neurons from both species; forward-propagating APs (fpAPs) had a different speed than backpropagating APs (bpAPs). Additionally, we observed distinct AP propagation characteristics in AISs emerging from the somatic envelope compared to those originating from dendrites. Compared with rat neurons, mouse neurons exhibited higher bpAP speed and lower fpAP speed, more distally located ankyrin G (AnkG) in AISs, and longer Nav1.2 lengths in AISs. Moreover, during AIS plasticity, AnkG and Nav1.2 showed distal shifts in location and shorter lengths of

Received: 16 May 2022; Accepted: 27 June 2022; Online: 27 June 2022
Foundation items: This work was supported by the National Science and Technology Innovation 2030-Major Program of “Brain Science and Brain-Like Research” (2022ZD0211800), National Natural Science Foundation of China General Research Grant (81971679, 21727806, 31771147) and Major Research Grant (91632305, 32088101), Ministry of Science and Technology (2018YFA0507600, 2017YFA0503600), Qidong-PKU SLS Innovation Fund (2016000663), and Fundamental Research Funds for the Central Universities and National Key R&D Program of China (2020AAA0105200). P.Z. was sponsored by the Bayer Investigator Award
*Corresponding authors, E-mail: taolt@mail.cbi.pku.edu.cn; zoupeng@pku.edu.cn; yanzhang@pku.edu.cn

labeled AISs in rat neurons; in mouse neurons, however, they showed a longer AnkG-labeled length and more distal Nav1.2 location. Our findings suggest that hippocampal neurons in SD rats and C57 mice may have different AP propagation speeds, different AnkG and Nav1.2 patterns in the AIS, and different AIS plasticity properties, indicating that comparisons between these species must be carefully considered.

Keywords: Sprague-Dawley rats; C57BL/6 mice; Action potential; Axon initial segment; Plasticity

INTRODUCTION

Neurons generate all-or-none action potentials (APs) at the axon initial segment (AIS), which is a specialized axonal compartment proximal to the soma (Bender & Trussell, 2012; Clark et al., 2009; Kole & Stuart, 2012). The AIS is a highly structured region consisting of scaffolding proteins (e.g., ankyrin G; AnkG), transmembrane cell adhesion molecules (e.g., neurofascin 186; NF-186), and a dense population of voltage-gated ion channels (Grubb & Burrone, 2010b; Rasband, 2010). The location and length of the AIS vary by neuronal type (Fried et al., 2009; Kuba et al., 2006), but how these properties affect AP generation and information transmission is not well understood.

APs are initiated at the AIS and propagate in two directions. Forward-propagating APs (fpAPs) travel along the axon toward the synaptic terminal and trigger neurotransmitter release into adjacent target neurons. In contrast, backpropagating APs (bpAPs) travel in the opposite direction toward the soma and dendrites. The interplay between bpAPs and input electrical signals has been implicated in long-term potentiation (Bashir & Collingridge, 1992; Kamal et al., 1999; Morris, 1989; Voronin, 1993). During this process, AP propagation speed critically affects the timing of electrical signals, which is key to triggering transmitter release at the axon terminals, integrating information with other synaptic signals at the soma, and responding to physiological fluctuations (Alle & Geiger, 2006; Debanne, 2004; Kole et al., 2007; Rama et al., 2018; Schmidt-Hieber et al., 2008; Shu et al., 2006). The AIS itself is not a rigid structure. Its length and location can be altered through short- and long-term changes in molecular components, functions, and neuronal excitability to adapt to the surrounding environment, a process known as AIS plasticity (Evans et al., 2015; Grubb & Burrone, 2010a; Grubb et al., 2011; Kuba et al., 2010, 2015; Leterrier, 2018; Yamada & Kuba, 2016). Both experimental manipulations and computational modeling have shown that AIS plasticity can significantly affect the efficiency of neuronal signaling (Kole & Stuart, 2012; Kuba et al., 2006; Muir & Kittler, 2014; Wang et al., 2011).

In mammals, including humans, the hippocampus is an ensemble of neurons called engrams (also known as memory traces) (DRaDR, 1922; Josselyn et al., 2015, 2017; Tonegawa et al., 2015) that are formed during learning and reactivated to drive memory recall. The robust functional plasticity of hippocampal neurons is presumed to be the most important factor contributing to the achievement of such memories (Morris et al., 1990). Many studies have been conducted on the anatomy, physiology, and function of CA1 pyramidal neurons in rats (Golding et al., 2005; Harris & Stevens, 1989; Jarrard, 1993; Megías et al., 2001; Poirazi et al., 2003; Wyass & Van Groen, 1992). However, with the recent development of genetic techniques, mice have become common models for studying the potential mechanisms underpinning learning and memory (Chen et al., 2006; Hickman-Davis & Davis, 2006; Nolan et al., 2004; Picciotto & Wickman, 1998; Rocha-Martins et al., 2015). Although mice are evolutionarily close to rats, significant differences exist between the species, which complicates direct comparisons. Notably, neurons from Sprague-Dawley (SD) rats and C57BL/6 (C57) mice may differ in total dendritic length, surface area, and volume, spatial distribution and branching of dendritic arbor, dendritic spine size and density, resting membrane potential (V_m), input resistance (R_N), membrane time constant (τ), and active membrane properties (Routh et al., 2009). However, it remains to be determined whether neurons from these species exhibit similar AP propagation speeds and AIS plasticity mechanisms.

Here, we combined voltage imaging with genetically encoded voltage indicators (GEVIs) and multicompartment electrophysiological modeling to map the dynamics of AP initiation and propagation in cultured hippocampal neurons derived from SD rats and C57 mice. Over the past decade, the development of GEVIs has enabled quantitative description of AP waveforms in small neuronal structures, such as the AIS (Antic, 2003; Foust et al., 2010; Hochbaum et al., 2014; Popovic et al., 2011). In the present study, we showed that APs were initiated near the distal end of the AIS and traveled bidirectionally at the AIS, with fpAPs and bpAPs exhibiting different speeds. Notably, bpAPs propagated more slowly in AISs originating from dendrites (“axon-carrying dendrites”) (Thome et al., 2014) than in AISs originating from the soma. Moreover, we observed differences in AP speed and AISs between rat and mouse neurons. Specifically, neurons from mice had a higher bpAP speed and a lower fpAP speed than neurons from rats. Compared with rat neurons, AnkG was located more distally and Nav1.2 staining was longer in the AISs of mouse neurons. Furthermore, during AIS plasticity, the rat neurons showed a distal location and shorter length of staining for both AnkG and Nav1.2; however, the mouse neurons showed a longer AnkG-labeled length and more distally located Nav1.2. Taken together, our data revealed the diversity of AP speed and AnkG/Nav1.2 patterns in the AISs of neurons in rats and mice and showed considerable differences in AIS plasticity between the two species, indicating that comparisons between SD rat and C57 mouse neurons must be carefully considered.

MATERIALS AND METHODS

Reagents, plasmids, and antibodies

Poly-D-lysine (PDL), Tween-20, Triton-100, Hanks’ balanced salt solution (HBSS), bovine serum albumin (BSA), fetal bovine serum, and fetal calf serum were obtained from Sigma

(USA). Dulbecco's Modified Eagle Medium (DMEM), neurobasal medium, GlutaMAX, B27 supplement, penicillin/streptomycin, and trypsin were obtained from Gibco (USA). Tyrode's salt solution was purchased from MACGENE (China). The FCK-QuasAr2-mOrange2 plasmid was a generous gift from Dr. Adam E. Cohen (Harvard University, USA). The anti-neurofascin antibody (extNF; A12/18, 75-172) and anti-Nav1.2 antibody (K69/3) were obtained from NeuroMab (USA). The anti-ankyrin G antibody (33-8800) was purchased from Invitrogen (USA). The anti-MAP2 antibody (ab5392) was obtained from Abcam (UK). Alexa Fluor® 405 goat anti-mouse, Alexa Fluor® 488 donkey anti-mouse, and Alexa Fluor® 568 donkey anti-chicken were purchased from Invitrogen (USA).

Animals

We obtained 24 postnatal day 0 SD rat pups and 18 postnatal day 0 C57BL/6J mouse pups from Beijing Vital River Laboratory Animal Technology Co., Ltd. (China). All animal handling, care, and experiments followed the rules and regulations of the Peking University Animal Care and Use Committee, as described previously (Cui et al., 2011; Sun et al., 2014).

Dissociation of hippocampal cultures

According to standard protocols, we prepared dissociated mixed neuronal and glial cultures from the hippocampus of postnatal day 0 rat/mouse pups. Briefly, hippocampi were dissected in DMEM, digested in 0.25% trypsin (15 min, 37 °C), triturated through Pasteur pipettes of increasingly narrow diameter, and plated at 60 000 cells/mL onto PDL (50 μg/mL)-coated glass-bottom dishes (Cellvis, China). Cultures were incubated (37 °C, 5% CO_2) in neurobasal medium containing B27 supplement, 2 mmol/L GlutaMAX, and penicillin/streptomycin. The medium was half-replaced after 48 h.

Transfection

Calcium phosphate transfection was used to introduce the QuasAr2-mOrange2 plasmid directly into the cell at day 8 *in vitro* (DIV7). Generally, for every dish, 2 μg of QuasAr2 plasmid in a 12.4 μL $CaCl_2$/water solution was mixed with 2×HEPES (Gibco, USA) balanced solution (pH 7.12), followed by gentle vortexing. A plasmid/calcium phosphate complex was formed after 10 min of incubation at room temperature and then dropwise added to DIV6 neurons prewashed with neurobasal medium on glass-bottom dishes. Cultures were incubated in a humidified 5% CO_2 chamber at 37 °C for 30 min, with precipitation observed around the cells. The precipitate was dissolved by adjusting the medium pH to 6.8, followed by incubation at 37 °C for 5 min. Finally, cells were fed with the original growth medium and maintained until DIV12 for live imaging, immunofluorescence, or other treatments, as described below.

AIS live-cell labeling

The mouse anti-pan-neurofascin antibody (extNF; A12/18, NeuroMab, USA) was generated against the rat-specific extracellular domain common to NF155 and NF-186 (amino acids 25–1 110). Cultured neurons at DIV12 were washed three times in HBSS and incubated with primary antibody solution (1:200) at 37 °C for 30 min. Next, cells were washed three times in HBSS and incubated with secondary antibody (anti-mouse 405, 1:500) at 37 °C for another 30 min. Finally, cells were washed and added with Tyrode's buffer for imaging.

Immunocytochemistry

The following primary antibodies were used: mouse anti-AnkG (1:500; 33-8800, Invitrogen, USA), chicken anti-MAP2 (1:10 000; ab5392, Abcam, UK), and mouse anti-Nav1.2 (1:200; K69/3, NeuroMab, USA). For AnkG and MAP2 labelling, cultures were fixed with 4% paraformaldehyde (20 min at room temperature) and incubated with primary antibody for 1 h at room temperature. For staining with the anti-Nav1.2 antibody, we used 2% paraformaldehyde for fixation (20 min at room temperature). Otherwise, all labelling steps were identical. After washing with Tyrode's buffer, permeabilizing in 0.2% Triton X-100 (5 min at room temperature), and blocking with 5% BSA (30 min at room temperature), the cells were incubated with primary antibody solution (in 5% BSA) for 1 h. The sample was then washed three times and stained with dye-conjugated secondary antibodies for 1 h at room temperature. Finally, the cultures were washed three times and transferred into Tyrode's buffer for imaging.

Imaging apparatus

Fluorescence imaging was performed on an inverted fluorescence microscope (Nikon-TiE, Japan) equipped with a 40×1.3 NA oil immersion objective lens, six laser lines (Coherent, USA) OBIS 405, 488, 532, 561, and 637 nm for confocal imaging, and high-intensity 637 nm for voltage imaging), spinning disk confocal unit (Yokogawa CSU-X1, Japan), and two scientific CMOS cameras (Hamamatsu ORCA-Flash 4.0 v2, Japan). The microscope, lasers, and camera were controlled with customized software written in LabVIEW (National Instruments, v15.0, USA) and could switch between confocal and widefield imaging modes. Imaging of staining and fluorescent proteins was performed at illumination intensities of 1–6 W/cm^2, while imaging of QuasAr2 was performed at 900 W/cm^2. Supplementary Table S1 summarizes the laser lines, dichroic mirrors, and emission filters used for fluorescence imaging.

Confocal imaging of neurons

After labeling, cultures were transferred to Tyrode's buffer. Images were acquired using 1×1 camera binning with an exposure time of 100–1 000 ms in Z-stack mode with a 0.3–0.5 μm step length. Each image stack was performed with Z-axis max intensity projection, and the new projected images in several channels were adjusted and merged with ImageJ/Fiji (NIH, USA)

Simultaneous patch-clamp recordings and fluorescence imaging

Hippocampal neurons from rats/mice were cultured, transfected, and labeled as described above. All imaging and electrophysiological analyses were performed in customized high-glucose Tyrode's buffer containing 125 mmol/L NaCl, 2.5 mmol/L KCl, 3 mmol/L $CaCl_2$, 1 mmol/L $MgCl_2$, 10 mmol/L HEPES, and 30 mmol/L glucose (pH 7.3), adjusted to 305–310 mOsm/kg with sucrose. The synaptic blockers D-

APV (25 μmol/L), NBQX (10 μmol/L), and gabazine (20 μmol/L) (all from Abcam, UK) were added to the imaging medium for single-cell measurement.

Electrophysiological experiments were performed at room temperature. Borosilicate glass electrodes (Sutter, USA) were pulled to a tip resistance of 2.5–5.0 MΩ. The glass electrode was filled with internal solution containing 125 mmol/L potassium gluconate, 8 mmol/L NaCl, 0.6 mmol/L $MgCl_2$, 0.1 mmol/L $CaCl_2$, 1 mmol/L EGTA, 10 mmol/L HEPES (from Sigma, USA), 4 mmol/L Mg-ATP, and 0.4 mmol/L Na_2-GTP (from Shanghai Yuanye Bio-Technology Co., Ltd., China) (pH 7.3), adjusted to 295 mOsm/kg with 1 mol/L sucrose (Sigma, USA). A Sutter MP285 micromanipulator (USA) was used to adjust the position of the glass electrode. The cells were clamped using an Axopatch 200B amplifier (Axon Instruments, USA). The membrane voltage signal recorded from the patch amplifier was filtered with an internal 5 kHz Bessel filter and digitized at 21 159.48 Hz (for Figure 1) or 9 681.48 Hz (for other figures) with a National Instruments PCIe-6353 data acquisition (DAQ) board (USA, approximately twice the bandwidth of the Bessel filter). Recordings with >10% change in membrane resistance during measurement were considered as failed patch clamp attempts and were discarded from further analysis.

To collect spike-triggered average movies from neurons expressing QuasAr2-mOrange2, we clamped cultured neurons in the whole-cell current-clamp mode (Axopatch 200B, Axon Instruments, USA). We stimulated neurons 80 or 125 times with a 10 ms 100 pA–500 pA current injection (stimulation frequency of 6 Hz or 4 Hz, respectively) and simultaneously recorded QuasAr2 fluorescence movies of the clamped neuron. The movies were acquired at a 484 Hz (2.0658 ms exposure time for each frame) or 1 058 Hz frame rate (0.9452 ms exposure time for each frame) in rolling-shutter mode with 2-by-2 binning, and the movies were averaged over all simulated APs (by peak finding and alignment) to boost the signal-to-noise (SNR) ratio for subsequent data interpolation and analysis. Camera bias (intensity of 400 in 2×2 binning mode) was subtracted from these average intensities to give final values. QuasAr2 and mOrange2 were imaged with a 637 nm laser line at an intensity of 900 W/cm^2 and 532 nm laser line at 1.0 W/cm^2, respectively. The SNR was defined as the ratio of maximum fluorescence change over the standard deviation of baseline fluorescence fluctuations. For all experiments, the fluorescence signal was corrected for the photobleaching effect. The photobleaching baseline was constructed from the whole field intensity by a sliding minimum filter, followed by a smooth processing algorithm. Each frame of the raw movie (after camera bias subtraction) was then divided by the photobleaching baseline.

Data analysis

To increase the SNR, neurons were stimulated 80–125 times. Data processing was performed to calculate the speed of axons during this periodic signal. Video data were processed using a self-developed method with MATLAB (Mathworks, vR2017a, USA).

The method flow chart is shown in Supplementary Figure S1A. Firstly, raw data were filtered using a Gaussian low-pass filter (size: 3×3, sigma: 1) to remove spatial noise. As shown in Supplementary Figure S1B, S1C, spatial filtering increased the contrast of the standard deviation image. Pixels with low standard deviations were defined as background pixels, while pixels with large standard deviations were defined as region of interest (ROI) pixels. Spatial filtering reduced the signals of background pixels and background noise. Next, as shown in Supplementary Figure S1D, the centerline of the axon was drawn (red line). We set a 5×5 region (white square) centered by each pixel on the centerline as the whole ROI (region circled by white line). We twice smoothed the intensity of the whole ROI to obtain the photobleaching baseline (Supplementary Figure S1E). The first smoothing was a minimum filtering (window size: 4×80), i.e., red line, and the second smoothing was mean filtering (window size: 2×80), i.e., yellow photobleaching baseline. The final normalized signal value was the intensity divided by the photobleaching baseline (Supplementary Figure S1E, lower). We then found the peaks (local maximum) of the periodic APs (Supplementary Figure S1F, upper) and averaged them to obtain mean AP (blue AP in Supplementary Figure S1F, lower). To increase time resolution, we interpolated the kernel with a cubic spline to obtain the green AP, which was used as a kernel to revise the APs on each segment. Based on cubic spline interpolation, time resolution of the data increased from 2 ms to 0.002 ms.

We calculated the arrival time of AP peaks on each segment. Each segment was defined by 21 pixels on the centerline. As shown in Supplementary Figure S1G, we averaged the pixel signals in the green region segment to the signal on the red point (green region center). The green region was a small window sliding on the centerline. We first interpolated the signal of the red point (blue signal), using cubic spline as the interpolation on the kernel. We then convolved the splined signal on the red point (red signal) with the kernel (green signal in Supplementary Figure S1F) to calculate the correlation coefficient (yellow line in Supplementary Figure S1G). We replaced the splined signal with the kernel according to the correlation coefficient and obtained the corrected signal (purple signal). We then used the corrected high-precision signal to find the AP peak arrival time of the red point. After the green window slides over all pixels on the centerline, we obtained the corrected APs and their peak arrival times at all locations of the axon.

Finally, we calculated the mean and instantaneous speeds. We linearly fit the points in Supplementary Figure S1H (lower right), with the slope of the line representing mean speed (Supplementary Figure S1I). AP propagation was always unidirectional. However, some raw data points were not monatomic due to imaging noise (Supplementary Figure S1J). Therefore, when calculating instantaneous speed, we fit the raw data using least-squares curve fitting with linear constraints, where C is the identity matrix, x is the unknown monotonic time, d is the raw data point (peak arrival time), and $x_{i+1} - x_i \leqslant 0.001$ is the constraint.

$$\min_x \frac{1}{2}||C \cdot x - d||_2^2 \quad \text{s.t.} \quad A \cdot x \leqslant b \tag{1}$$

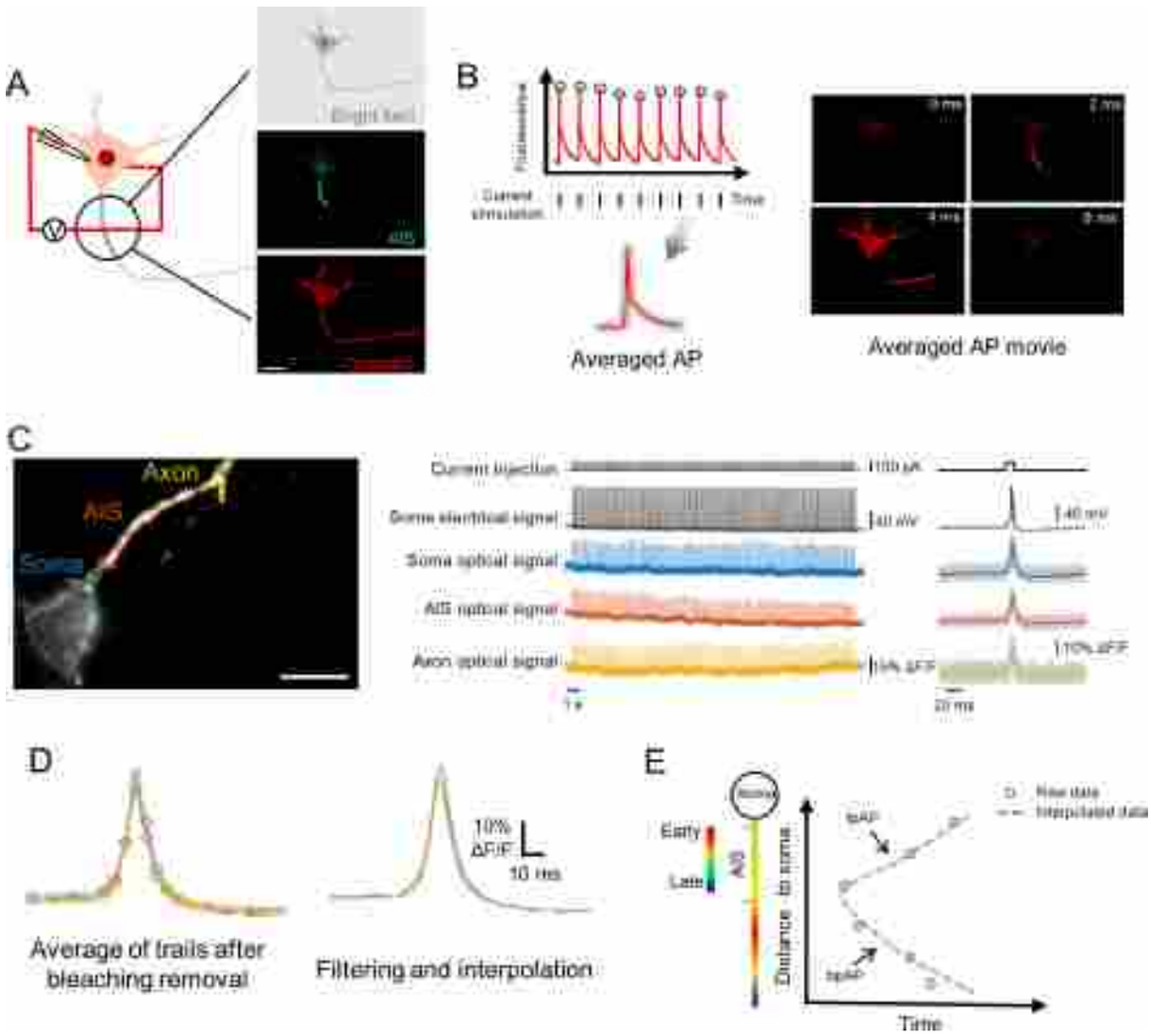

Figure 1 Well-resolved AP initiation and propagation at AISs via voltage imaging

A: Illustration of AIS identification in a neuron after voltage imaging under a microscope. B: Spike-triggered average movie for average AP waveform of each pixel in field of view for the following interpolation. C: Left, cell expressing QuasAr2-mOrange2 was selected and AP train was recorded after current stimulation of the soma, and different regions of interest (ROI) in the neuron in the field-of-view were polygonally outlined in different colors, corresponding to traces in the middle column; Middle, signals of recorded somatic electrophysiological data and corresponding voltage imaging data of selected cells. Injected current (200 pA 10 ms, 4 Hz, shown with gray line) evoked AP trains (electrical signal in soma, gray). Corresponding optical voltage signals were simultaneously recorded with an sCMOS camera in good synchronization (blue: soma; orange: AIS; yellow: axon). Sub-threshold electrical event (failed APs) was well-removed in the traces; Right, average electrical AP trace (black line on top) and optical traces of average AP signals (blue: soma; orange: AIS; yellow: axon) evoked by somatic stimulation (black line on bottom). Average traces were superimposed with single AP trails (gray backward lines). D: Left, superimposed average signals of three ROIs in Supplementary Figure S2B acquired at 484 Hz. Circle markers on solid lines indicate raw optical data points; Right, corresponding 1 000 times upsampled optical signal via a maximum correction-based waveform filter and cubic spline-based interpolation algorithm (interval=2.0658 μs) (Supplementary Figure S4 and Methods). E: According to high spatiotemporal AP initiation and propagation mapping from voltage imaging and interpolation, AIS parameters (e.g., length, distance to soma, and width, left column) and AP propagation details (AP initiation site, bidirectional propagation speed at AIS, soma, axon, and neighbor dendrites, right column). Circles in the right figure represent AP arrival time calculated from original voltage imaging movie. Dashed lines represent AP arrival time from interpolated data.

Generally, the maximum speed at the AIS was 300 μm/ms and minimum distance between two data points was 0.325 μm (pixel size in raw imaging data). The constraint was set to 0.001, and we calculated the monotonic propagation line. The slope of the line at each location was the instantaneous speed. The speed change per unit distance was equivalent to acceleration.

The spatial and temporal resolutions of speed were 0.325 μm (along propagation direction at axon) and 0.002 ms, respectively. We defined propagation speed as peak

propagation speed. Due to the limitations of the raw data and analysis methods, speed calculations at the AIS shorter than 20 μm were not precise enough. Therefore, only AISs longer than 20 μm were quantitatively observed. The data processing code is available at GitHub (https://github.com/Jessie940611/Action-Potential-Propagation-Velocity-is-Influenced-by-AIS-Plasticity).

Multi-compartmental modeling

We created a detailed multi-compartment model of a neuron to explore the relationship between neuronal morphology and AP propagation speed. The model included simplified morphology, ion channel distributions and densities, channel kinetics, and passive properties. We stimulated the model neuron with a pulse current injected directly into the soma. Simulation was performed using the Python (v3.6.6) interface in Neuron (v7.6.5). The integration time steps were fixed at 0.001 ms. The length of the segments was 1 μm. The simulation code is available at GitHub (https://github.com/Jessie940611/Action-Potential-Propagation-Velocity-is-Influenced-by-AIS-Plasticity).

Neuronal morphologies included several simple cylinders to mimic dendrite, soma, hillock, AIS, and axon. Passive parameter values were optimized within physiologically relevant ranges from the literature (Mainen & Sejnowski, 1998; Saraga et al., 2003). The values of passive parameters were selected to match the experimentally measured input resistance and membrane time constant in the hippocampal neurons. For active properties, the gating kinetics of voltage-dependent Nav and Kv channels were Hodgkin-Huxley style (Hu et al., 2009). The densities of ion channels were set according to previously published values (Hu et al., 2009; Saraga et al., 2003). The model parameters are listed in Supplementary Tables S2, S3.

RESULTS

Spatiotemporally resolved voltage imaging of AP propagation at AIS

We selected QuasAr2 as the GEVI due to its superior sensitivity (90% $\Delta F/F_0$ per 100 mV) and fast response kinetics (Hochbaum et al., 2014). This indicator has been employed to monitor AP initiation in cultured rat hippocampal neurons (Hochbaum et al., 2014) and to investigate the neuronal excitability of patient-derived motor neurons (Kiskinis et al., 2018). Compared to previous AIS imaging studies (Antic, 2003; Foust et al., 2010; Popovic et al., 2011), QuasAr2 provides a superior SNR due to its lower background signal and higher voltage sensitivity (Bando et al., 2019; Xu et al., 2017). As shown in Figure 1A, cultured rat hippocampal neurons were transfected with the QuasAr2-mOrange2 plasmid. The AIS was visualized with immunofluorescence staining for the neurofascin-186 (NF-186) marker protein. Neurons were then stimulated using the whole-cell current clamp technique, in which periodic current injections into the soma triggered AP firing. Concurrently, a QuasAr2 fluorescence image series was acquired at a 1 000 Hz frame rate (Figure 1B). The resulting voltage imaging movie robustly detected AP spikes at the AIS and neighboring regions. In the AIS, AP spikes were detected with a remarkable SNR ranging from 11 to 36 (Figure 1C, outlined AIS region; mean±standard deviation: 17.2±4.3). The SNR was increased to 111 by averaging the AP spikes (Figure 1C, right column, AIS trace). We adapted a digital upsampling algorithm (Hochbaum et al., 2014; Popovic et al., 2011) to analyze AP timing with sub-millisecond-level temporal resolution and pixel-level spatial resolution (Figure 1D, E; Supplementary Figure S1).

Voltage imaging of AP propagation speed at AIS

In this study, *AIS length* was defined as the distance between the proximal and distal ends of each AIS, and *AIS location* was defined as the distance from the soma to the proximal end of the AIS (Grubb & Burrone, 2010a) (Figure 2A). Following onset at the AIS, APs propagated bidirectionally, with fpAPs traveling along the axon and bpAPs traveling back toward the soma and dendrites (Figure 2A, B). The AIS region was identified with the fluorescently labeled NF-186 marker protein (Figure 2B, left panel). Fluorescence intensity of each image was smoothed and normalized. The AIS boundary at both the proximal and distal ends was defined as the location where NF-186 fluorescence intensity decreased to 10% of the maximum at the AIS (Grubb & Burrone, 2010a).

First, we determined the AP initiation site at the AIS (Figure 2B). The initiation sites of individual APs were identified from the voltage imaging data. We normalized the AIS lengths and found that AP initiation sites occurred with the highest frequency at 50%–70% along the AIS, slightly biased to the distal end (Figure 2C). This bias in location is consistent with the spatial distribution of the voltage-gated sodium channel Nav1.6 in the AIS (Hu et al., 2009)

After initiation, both bpAPs and fpAPs were generated and traveled at different speeds. The speed of the fpAPs was 1.87±0.39 times higher at the AIS than at the more distal axon (119.5±18.7 μm/ms versus 73.45±7.76 μm/ms, respectively, *: $P<0.05$) (Figure 2D, left panel, and Figure 2E). On average, the fpAPs traveled 1.51±0.18 times faster than the bpAPs (112.6±14.2 μm/ms versus 84.99±7.59 μm/ms, ns: $P>0.05$) (Figure 2D, right panel, Figure 2F). Thus, voltage imaging enabled us to distinguish AP propagation speed in different subcellular regions. Furthermore, neither AIS location (Figure 2G) nor AIS length (Figure 2H) affected bpAP speed ($n=30$). In contrast, fpAP speed ($n=19$) was significantly lower at distal and shorter AISs (Figure 2I, J).

Influence of AIS length and location on fpAP propagation speed

Results revealed that fpAP speed was significantly correlated with AIS location and length (Figure 2I, J). We pharmacologically perturbed the AIS in neurons to verify the relationship between fpAP speed and AIS location. Previous research has shown that treating mature AISs (after DIV7) with KCl (15 mmol/L for 48 h) can significantly shift the AIS distally without affecting AIS length (Grubb & Burrone, 2010a). We applied this method to induce a shift in the AIS location. After treatment with 15 mmol/L KCl from DIV10 to DIV12, neuronal resting potential was unchanged (Figure 3A), while rheobase increased significantly when neurons were allowed to recover in 2.5 mmol/L K^+ extracellular medium (Figure 3B).

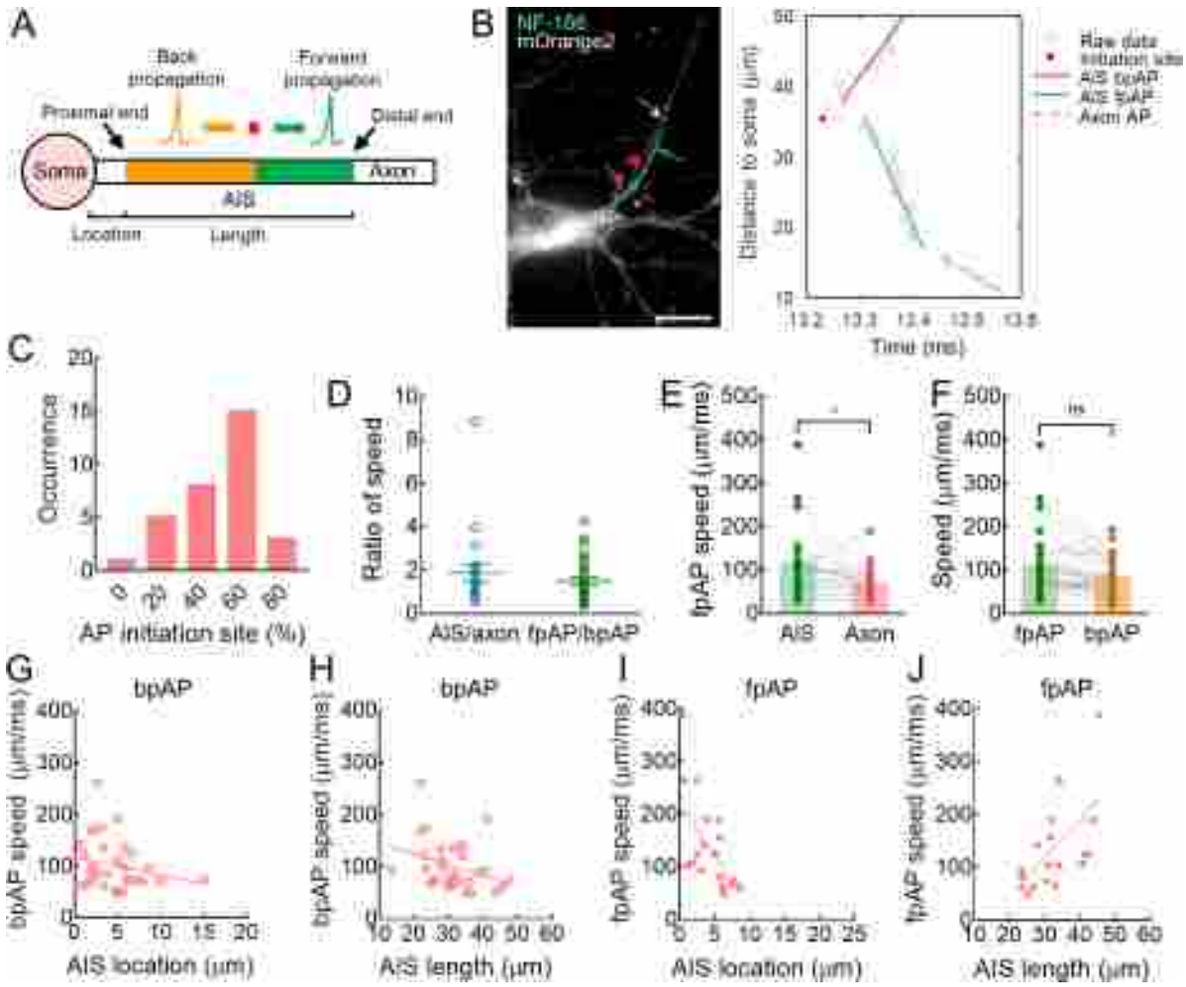

Figure 2 AP speed varied during propagation

A: Schematic of a neuron, including soma, AIS, and axon. AIS location was defined as distance from the soma to AIS proximal end. AIS length was defined as distance from the proximal end to distal end. AP was initiated at the initiation site (red star) and propagated backward (orange) and forward (green). B: Left, representative image of AIS of DIV12-cultured hippocampal neurons from rat expressing QuasAr2-mOrange2. Fluorescence of mOrange2 (white) and NF-186 (blue) denotes whole cell and AIS, respectively. Red dot denotes AP initiation site (same as map on right side). Arrows denote axon compartments, and corresponding AP propagations are shown in the right chart with different colored lines. Right, slopes of fitted lines are average speed. AP propagation speed on AIS compartments differed after AP initiation (Scale bars: 20 μm). C: Histogram of relative AP initiation site at AIS, mean=48.06%±3.28%, n=32. D: Paired comparison of fpAP speed at AIS/axon (number of pairs=21, mean=1.871±0.39), and paired comparison of fpAP speed/bpAP speed at AIS (number of pairs=29, mean=1.507±0.16). E: Paired comparison of fpAP speed at AIS and axon (number of pairs=21, mean speed at AIS=119.5±18.64 μm/ms, mean speed at axon=73.45±7.76 μm/ms, *: P<0.05). F: Paired comparison of fpAP and bpAP speed at AIS (number of pairs=29, mean bpAP speed=84.99±7.6 μm/ms, mean fpAP speed=112.6±14.2 μm/ms, ns: P>0.05). G: Correlation of AIS location and bpAP speed (n=30, r=−0.224, ns: P>0.05). H: Correlation of AIS length and bpAP speed (n=30, r=−0.334, ns: P>0.05). I: Correlation of AIS location and fpAP speed (n=19, r=−0.603, **: P<0.01). J: Correlation of AIS length and fpAP speed (n=19, r=0.579, **: P<0.01). Error bars represent standard error of the mean (*SEM*), two-tailed paired t-test was employed in D−F, and linear regression was employed in G−J.

As predicted, AIS location in these neurons shifted markedly from the soma (Figure 3C, D), but AIS length remained unchanged (Figure 3C, E). Consistent with the above observations (Figure 2G–J), bpAP speed showed little change in these neurons compared to the untreated neurons (99.46±14.94 μm/ms and 83.74±13.89 μm/ms, respectively, ns: P>0.05) (Figure 3F), while fpAP speed was much lower in these neurons compared to the untreated neurons (147.4±26.33 μm/ms and 65.33±9.30 μm/ms, respectively, *: P<0.05) (Figure 3G). In the KCl-treated group (n=15), AIS location and length did not significantly alter bpAP speed (Figure 3H, I). In contrast, fpAP speed (n=10) was negatively correlated with AIS location and positively correlated with AIS length (Figure 3J, K) in the KCl-treated neurons (Figure 3G–J). Thus, shifting the AIS distally did not significantly alter bpAP speed but significantly affected fpAP speed. Based on these results, AIS location and length influenced fpAP speed.

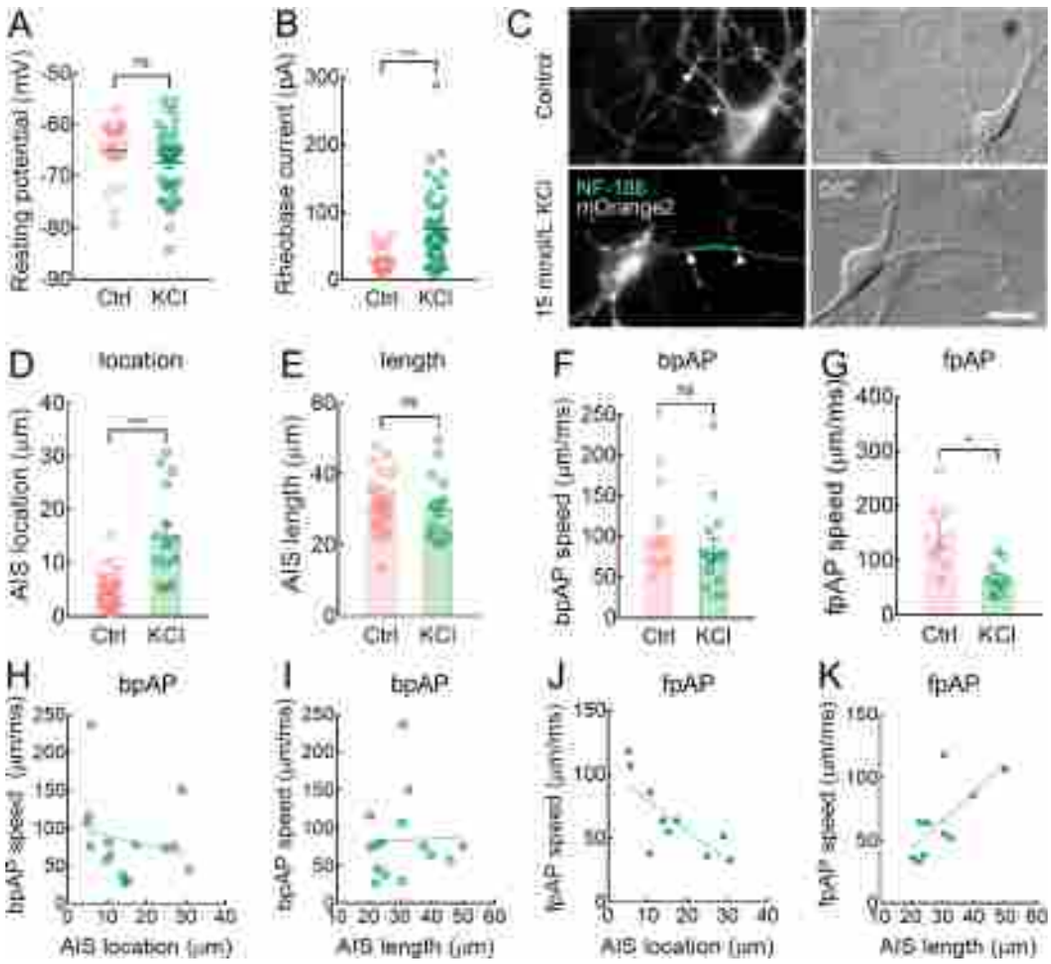

Figure 3 fpAP speed was negatively correlated with AIS location and positively correlated with AIS length

A: No significant difference was observed in resting potential of neurons in control group (−64.9±1.2 mV, *n*=22) and chronic KCl-treated group (−67.5±0.97 mV, *n*=46), ns: *P*>0.05. B: KCl treatment (15 mmol/L for 48 h) significantly increased rheobase current (76.18±7.718 pA, *n*=46) of neurons compared to control group neurons (29.55±3.877 pA, *n*=22), ***: *P*<0.001. C: Representative images of cultured wild-type rat hippocampal neurons (DIV12) without treatment (control, upper) and with KCl treatment (15 mmol/L for 48 h, lower). All neurons were transfected in DIV7 with QuasAr2-mOrange2 plasmid. (Left) Selected neurons (white) and their AISs (blue) are indicated by fluorescence of mOrange2 and axonal marker NF-186, respectively; (Right) Corresponding differential interference contrast (DIC) images of neurons in left column (Scale bars: 20 μm). D: Comparison of AIS location (AIS distance to soma). AIS was significantly further from the soma in KCl treatment group (15 mmol/L for 48 h) (14.98±2.30 μm, *n*=15) compared to control group (6.76±0.85 μm, *n*=45), ***: *P*<0.001. E: No significant difference in AIS length was observed between control group (32.51±1.16 μm, *n*=45) and KCl treatment group (15 mmol/L for 48 h) (30.26±2.40 μm, *n*=15), ns: *P*>0.05. F:No significant difference was observed in bpAP speed at AIS of control group neurons (99.46±14.94 μm/ms, *n*=10) and KCl treatment group neurons (15 mmol/L for 48 h) (83.74±13.89 μm/ms, *n*=15), ns: *P*>0.05. G: fpAP speed at AIS in KCl treatment group neurons (15 mmol/L for 48 h) (65.33±9.30 μm/ms, *n*=10) was lower than that in control group (147.4±26.33 μm/ms, *n*=7), *: *P*<0.05. H−K: Correlation between bpAP/fpAP speed and AIS location/length: Correlation between bpAP speed and AIS location (*n*=15, r=−0.210, ns: *P*>0.05) (H); Correlation between bpAP speed and AIS length (*n*=15, r=0.038, ns: *P*>0.05) (I); Correlation between fpAP speed and AIS location (*n*=10, r=−0.765, **: *P*<0.01) (J); Correlation between fpAP speed and AIS length (*n*=10, r=0.702, *: *P*<0.05) (K). Error bars represent *SEM*; two-tailed unpaired *t*-test was employed in A, B and D−G, and linear regression was employed in H−K.

bpAP speed was higher at dendrites than at AISs

In the cultured neurons, approximately 20% of neuronal AISs had a dendritic origin, consistent with previous observations of pyramidal cells in rats (Lorincz & Nusser, 2010; Thome et al., 2014; Triarhou, 2014). According to recent study, axons emanate from the basal dendritic arbor in more than half of all CA1 pyramidal neurons and 30% of those in rat pups (Thome et al., 2014). In the current study, “dendritic AISs” refer to AISs with a dendritic origin, whereas “somatic AISs” refer to AISs with a somatic origin (Figure 4A). In neurons with dendritic AISs, bpAP speed at the dendrite was 2.55±0.61 times higher than that at the AIS (116.5±26.0 μm/ms and 45.56±3.85 μm/ms, respectively, **: *P*<0.01) (Figure 4B, C).

As shown in Figure 4D, we constructed a multicompartment model to simulate a dendritic AIS neuron. The modeled neuron had two dendrites, one of which had a dendritic AIS

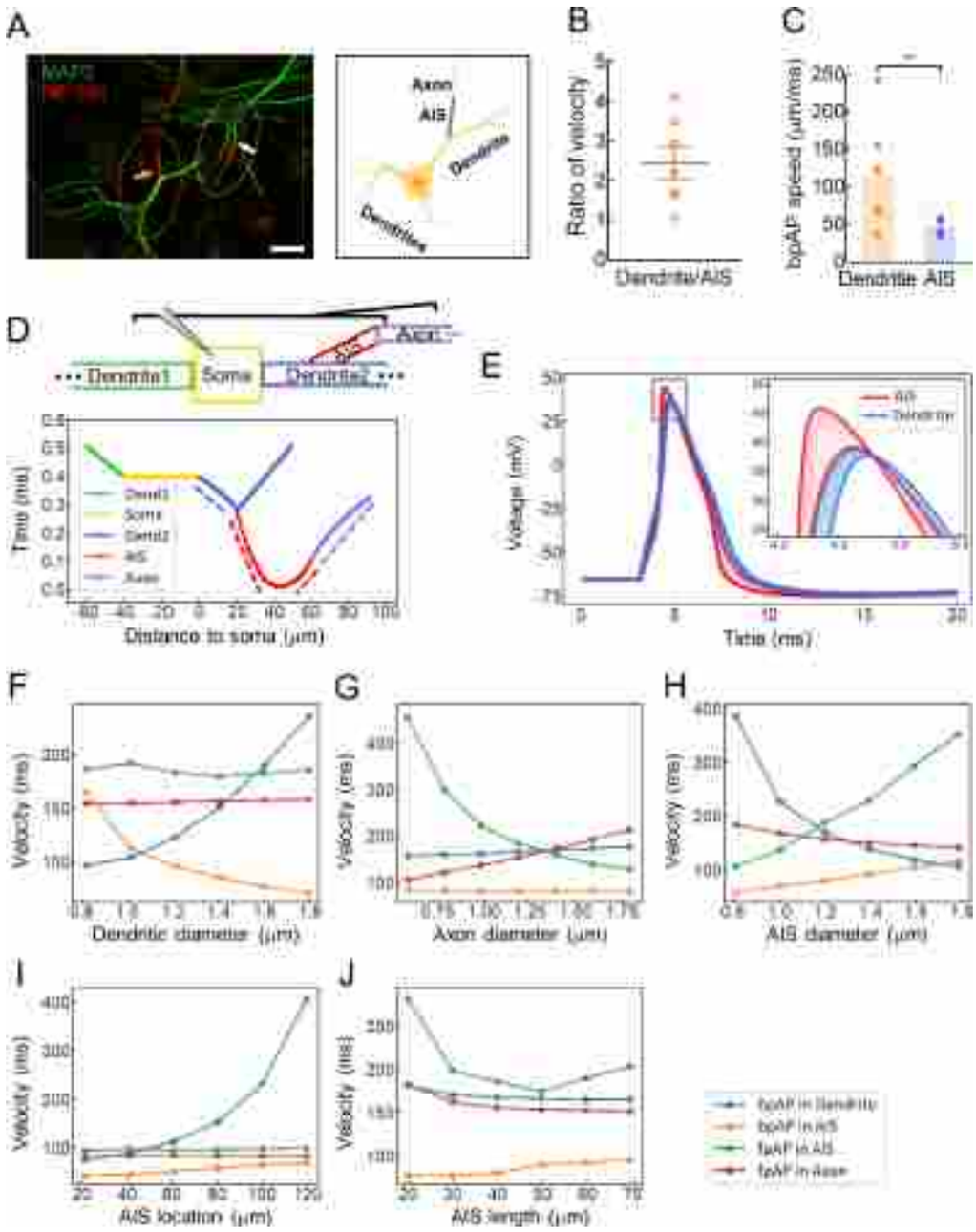

Figure 4 In dendritic AIS neurons, bpAP speed was lower at AISs than at corresponding dendrites

A: Left, immunofluorescence imaging of hippocampal neurons, white dotted circle and white arrow denote somatic AIS neuron and somatic AIS, respectively; yellow dotted circle and yellow arrow denote neuron with AIS originating from a dendrite (dendritic AIS neuron) and dendritic AIS, respectively (Scale bars: 20 μm). Right, schematic of dendritic AIS neuron. AIS is marked blue, others are yellow. B: Speed ratio of bpAP at corresponding dendrite and AIS. Number of pairs=7, mean=2.444±0.42. C: Paired comparison of bpAP speed at corresponding dendrite and AIS. Speed bpAP at dendrite (yellow dots) was significantly faster than that at AIS (blue dots) (number of pairs=7, **: P<0.01). D: Upper, schematic of multi-compartment dendritic model, depicting all neuronal compartments and injected stimulus in simulation. Soma (20 μm×40 μm) was attached to two dendrites (2 μm×1 000 μm). AIS (1.2 μm×10~70 μm) and axon (1.2 μm×1 000 μm) were attached to one dendrite. Stimulus was a 1 nA current that lasted for 1 ms. Current stimulus was injected into center of soma. Lower, arrival time of AP peaks on segments labeled by black line in dendritic model. Different sections are shown in different colors. Slopes of dashed lines are mean speed in different compartments. E: bpAPs at AIS (red) and dendrite (blue). Inner image shows peaks of APs. F−J: Regulatory effects of each parameter on conduction speed in each component. Each subgraph is modulation of (a) location of axon initiation node (i.e., axon initiation is distance between proximal end of node and soma), (b) length of axon starting node, (c) diameter of axon, (d) diameter of dendrite 2, and (e) axon initiation segment diameter on conduction speed in each compartment. Blue, yellow, green, and red data represent dendritic bpAP speed, AIS bpAP speed, AIS fpAP speed, and axonal fpAP speed, respectively. Error bars represent *SEM*; two-tailed paired *t*-test was employed in B, C.

with the proximal end located 20 μm from the soma. All compartments contained voltage-gated Na^+ and K^+ channels. The channel densities and compartment dimensions are shown in Supplementary Table S2. The arrival times of AP peaks in each segment are shown in Figure 4E, with different sections labeled in different colors. The mean propagation speed in each compartment was calculated by dividing the length of the compartment by the AP propagation time in that compartment (dotted line slope in Figure 4D. In this model, the bpAP speed was 168 μm/ms at the dendrites and 77.7 μm/ms at the AIS; the fpAP speed was 186 μm/ms at the AIS and 155 μm/ms at the axon. Thus, fpAP speed was lower at the axons than at the AIS; fpAP speed was higher than bpAP speed at the AIS; and bpAP speed was higher at the dendrites than at the AIS. These modeling trends were highly consistent with our experimental findings.

We also explored the effects of compartment morphology on speed by changing the dendritic diameter (Figure 4F), axon diameter (Figure 4G), AIS diameter (Figure 4H), AIS location (Figure 4I), and AIS length (Figure 4J) in the model. Dendritic diameter mainly influenced bpAP speed at the dendrites and AIS, axon diameter influenced fpAP speed at the AIS and axon, AIS diameter influenced fpAP and bpAP speeds in all segments, AIS location mainly influenced bpAP speed at the dendrites, and AIS length influenced fpAP speed at the AIS. Overall, speed was highly dependent on neuronal morphology.

bpAP speed was lower at dendritic AISs than somatic AISs

We next explored whether AIS origin affected AP speed. Overall, a much higher bpAP speed was observed at somatic AISs than at dendritic AISs (99.47±11.35 μm/ms and 55.65±7.85 μm/ms, respectively, *: P<0.05) (Figure 5A). However, dendritic and somatic AISs had comparable fpAP speeds (137.5±52.43 μm/ms and 91.13±19.42 μm/ms, respectively, ns: P>0.05) (Figure 5B). The lengths of the somatic and dendritic AISs were also similar (30.54±1.14 μm and 32.21±1.51 μm, respectively, ns: P>0.05) (Figure 5C, D).

We constructed two simplified models to clarify why bpAP speeds were faster at somatic AISs than at dendritic AISs. According to the Rall model, two cylinders (d_k representing diameter of k^{th} cylinder) were equivalent to one cylinder (diameter d_0) if

$$\sum_k d_k^{3/2} = d_0^{3/2} \quad (2)$$

In Figure 5E, the gray models represent the original models, and the pink and orange models represent the simplified equivalent models (Supplementary Figure S2B). As the axon hillock was thinner than the equivalent cylinder of two dendrites, the diameter of the middle compartment in the somatic AISs (2 μm) was correspondingly thinner than that of the dendritic AISs (3 μm). We focused on the effect of different AIS origins on AP propagation speed by setting uniform ion channel densities along the AIS. The stimulus (1 nA for 1 ms) was injected into the left end of the model. APs in both models were simultaneously initiated at the right end of the model. The solid and dotted lines represent APs at the somatic and dendritic AISs, respectively (Figure 5F). The AP peak reached the end of the somatic AISs earlier than the end of the dendritic AISs, indicating higher speed at the somatic AISs than at the dendritic AISs. Because APs at the dendritic AISs traveled through thicker cables than those at the somatic AISs, speed was expected to be lower at the dendritic AISs (Goldstein & Rall, 1974); this explains why bpAP speed was lower at the dendritic AISs than at the somatic AISs (Figure 5A).

After pharmacologically perturbing the AIS location in neurons by treating mature AISs (after DIV7) with 15 mmol/L KCl for 48 h, both somatic and dendritic AISs shifted distally without changes in length (Figure 3C–E; Supplementary Figure S2A). In addition, bpAP speed at the somatic and dendritic AISs did not differ significantly between the untreated and KCl-treated groups (Figure 3F, 5A). As shown above, bpAP speed of the dendritic AISs was notably lower than that of the somatic AISs (Figure 5A). Therefore, bpAP speed was more sensitive to axon origin (i.e., whether AIS was somatic or dendritic) than AIS location. However, fpAP speed at the somatic AISs was significantly higher in the control group than in the KCl-treated group (Figure 3G), with fpAP speed at the dendritic AISs exhibiting the same trend (Figure 5B). Moreover, fpAP speed did not differ between the somatic and dendritic AISs (Figure 5B). Thus, fpAP speed was more sensitive to AIS location than to axon origin. In terms of fpAPs, previous studies have shown that ion channel distribution (especially that of Nav1.2, Nav1.6, and Kv7.3) at the AIS and proximal areas of the axon may modulate fpAP conduction speed along the axon (Atherton et al., 2008). Our study revealed significant differences in Nav1.2 length/location between the somatic and dendritic AIS neurons (27.98±1.44 μm and 22.65±1.57 μm, respectively, *: P<0.05) (Figure 5G, H).

Hippocampal neurons from C57 mice had higher bpAP speed and lower fpAP speed than neurons from SD rats

We further examined whether hippocampal neurons from C57 mice had similar AP propagation characteristics to hippocampal neurons from SD rats. After voltage imaging, we used a standard immunofluorescence technique to visualize the recorded neurons and their AISs (Figure 6A). The neurons were filled with biocytin (0.5% w/v), and AnkG or NF-186 localization indicated AISs. The AP speeds in both directions were similar in mouse and rat neurons. Specifically, at the dendritic AISs, bpAP speed at the dendrites was generally higher than that at the AIS (115.4±16.97 μm/ms and 74.98±15.87 μm/ms, respectively, *: P<0.05) (Figure 6B). In addition, bpAP speed at the somatic AISs was also much higher than that at the dendritic AISs (135.0±14.61 μm/ms and 64.24±8.10 μm/ms, respectively, **: P<0.01) (Figure 6C), while fpAP speed at the somatic AISs was similar to that at the dendritic AISs (77.16±10.27 μm/ms and 75.18±24.62 μm/ms, respectively, ns: P>0.05) (Figure 6D).

In the somatic AIS neurons, bpAP speed was much higher in mice than in rats (88.22±8.62 μm/ms and 131.3±14.08 μm/ms, respectively, *: P<0.05), whereas fpAP speed was slightly lower (141.3±33.57 μm/ms and 82.92±11.73 μm/ms, respectively, ns: P>0.05) (Figure 6E, F). Based on

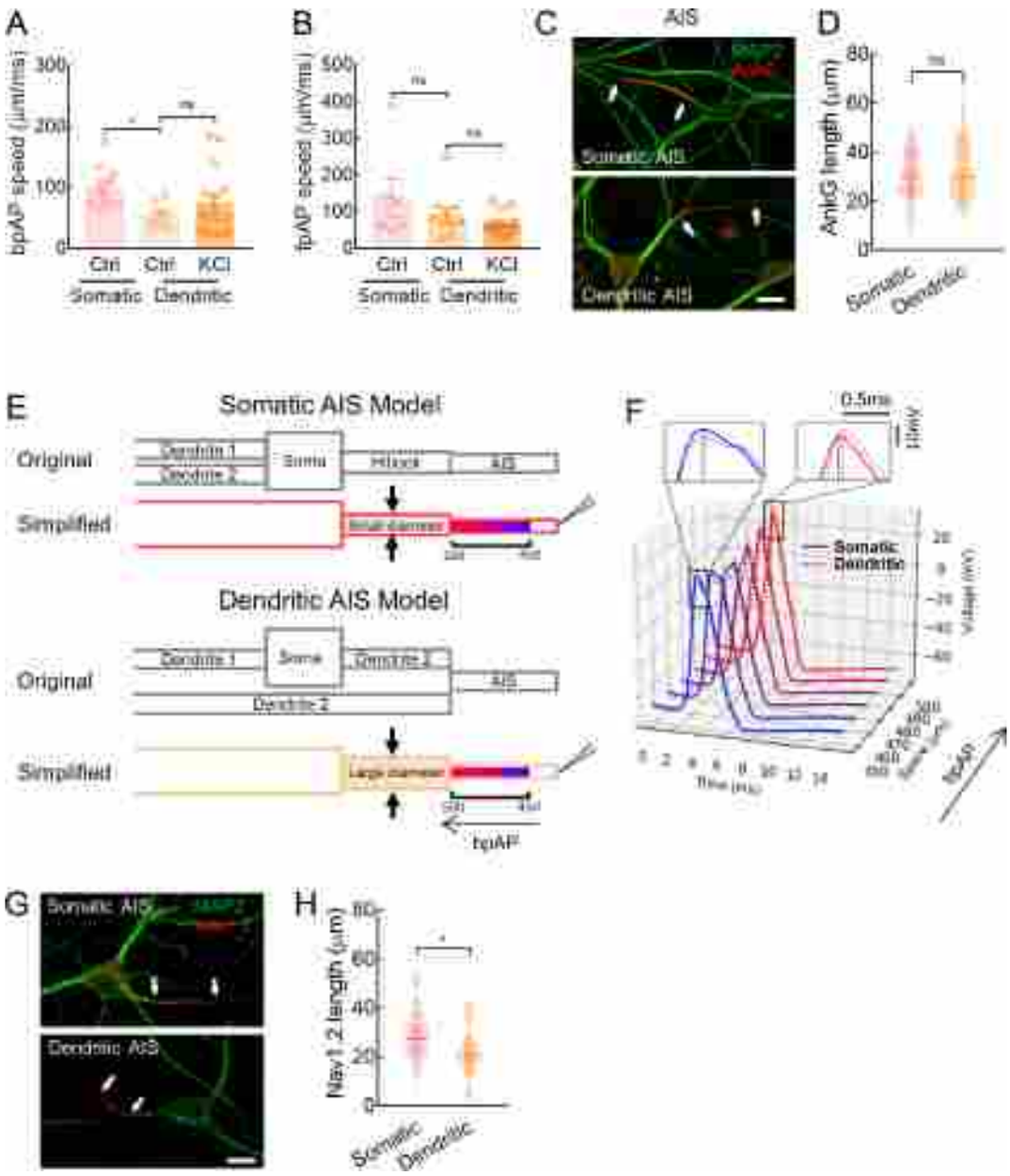

Figure 5 bpAP speed was lower at dendritic AISs than somatic AISs

A: Speed of bpAP at somatic AISs (pink circles, 99.47±11.35 μm/ms, *n*=10) was much higher than that at dendritic AISs (light orange circles, 55.65±7.85 μm/ms, *n*=7), *: *P*<0.05; at dendritic AISs, bpAP speed showed no difference between untreated group and KCl treatment group (dark orange circles, 73.26±13.35 μm/ms, *n*=16), ns: *P*>0.05. B: Speed of fpAP at somatic AISs (pink circles, 137.5±52.43 μm/ms, *n*=6) was similar than that at dendritic AISs (light orange circles, 91.13±19.42 μm/ms, *n*=10), ns: *P*>0.05; at dendritic AISs, fpAP speed showed no difference between untreated group and KCl treatment group (dark orange, KCl treatment group, 66.52±7.78 μm/ms, *n*=15), ns: *P*>0.05. C: Immunofluorescence images of AIS length indicated by AnkG, distance between two white arrows represents AIS length (Scale bars: 20 μm). D: Length indicated by AnkG between somatic AISs (30.54±1.14 μm, *n*=45) and dendritic AISs (32.21±1.51 μm, *n*=42) was similar, ns: *P*>0.05. E: Reformed multi-compartment neuronal models and their simplified equivalent cables. Stimulus was a 1 nA current that lasted for 1 ms. Stimulus was injected into one end of the thin cable. In the somatic model (pink), the three cables were 20 μm×50 μm (left), 2 μm×50 μm (middle), and 1.2 μm×500 μm (right). In the dendritic model (orange), the three cables were 20 μm×50 μm (left), 3 μm×50 μm (middle), and 1.2 μm×500 μm (right). Middle cable in dendritic model was thicker than that in the somatic model because the equivalent cable of two dendrites was thicker than one hillock. F: APs in 450–500 μm (AIS) of the model. Solid and dashed lines represent data of somatic and dendritic neuronal models. Peak of the first and last APs are magnified to see peak time. G: Immunofluorescence images of AIS length indicated by Nav1.2, distance between two white arrows represents Nav1.2 length (Scale bars: 20 μm). H: Length indicated by Nav1.2 between somatic AIS (27.98±1.44 μm, *n*=30) and dendritic AISs (22.65±1.57 μm, *n*=27) was similar, *: *P*<0.05. Error bars represent *SEM*; two-tailed unpaired *t*-test was employed in A, B, D, H.

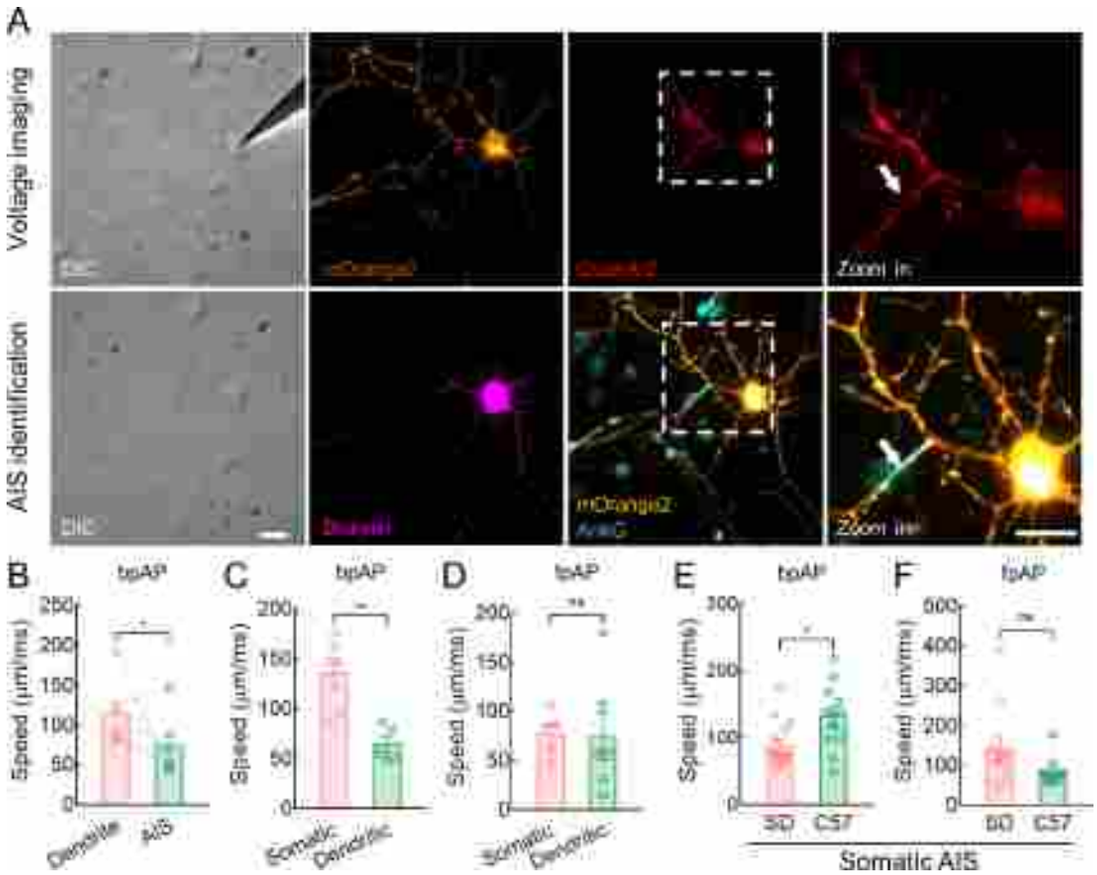

Figure 6 Mice neurons exhibited higher bpAP speed and lower fpAP speed than rat neurons

A: Fluorescence images of identical fields of view capturing step of voltage imaging (upper) and AIS identification (lower, after standard immunofluorescence). The highlighted 80 μm×80 μm regions (white lines) in the third column from the left are magnified in right column, showing QuasAr2 (upper, for voltage imaging) and mOrange2/AnkG (lower, for AIS identification), respectively. The co-localized region in QuasAr2 and AnkG was defined as the AIS for AP initiation and propagation analysis (Scale bars: 20 μm). B: Neurons from mice. Paired comparison of bpAP speed at corresponding dendrite and AIS. bpAP speed at dendrite (pink circles) was significantly higher than that at AIS (green circles) (number of pairs=6, *: P<0.05). C: Neurons from mice. bpAP speed at somatic AISs (pink circles, 135.0±14.61 μm/ms, n=6) was much higher than that at dendritic AISs (green circles, 64.24±8.10 μm/ms, n=5), **: P<0.01. D: Neurons from mice. fpAP speed at somatic AISs (pink circles, 77.16±10.27 μm/ms, n=5) was similar to that at dendritic AISs (green circles, 75.18±24.62 μm/ms, n=6), ns: P>0.05. E: In somatic AISs, bpAP speed at AISs in rat neurons (pink circles, 88.22±8.62 μm/ms, n=15) was lower than that in mouse neurons (green circles, 131.3±14.08 μm/ms, n=12), *: P<0.05. F: In somatic AISs, fpAP speed at somatic AISs (pink circles, 141.3±33.57 μm/ms, n=10) was similar to that at dendritic AISs (green circles, 82.92±11.73 μm/ms, n=10), ns: P>0.05. Error bars represent *SEM*; two-tailed unpaired t-test was employed in B−F.

AnkG localization, the AIS was significantly more distal in mouse neurons than in rat neurons, although AIS length was similar in both (Figure 7A, B). Consistent with previous study, the distally located AISs corresponded to lower fpAP speeds and similar bpAP speeds at the AIS (Figure 3D–G). Nav1.2 was located distally and was more widely distributed in the AIS of mouse neurons compared to rat neurons (Figure 7C, D). This distal shift in AIS and longer Nav1.2 may contribute to the lower fpAP speed and higher bpAP speed in C57 mouse neurons (Figure 7E).

Furthermore, we compared speed at the dendritic AISs in rat and mouse hippocampal neurons. Both bpAP speed (62.32±10.16 μm/ms and 68.63±16.14 μm/ms, ns: P>0.05) and fpAP speed (90.30±12.23 μm/ms and 87.27±18.37 μm/ms, ns: P>0.05) at the dendritic AISs were similar in rats and mice (Figure 7F, G). Unlike somatic AISs, AnkG length and location were similar in the dendritic AIS neurons of rats and mice (Figure 7H). However, we discovered a similar length but differences in distal location of Nav1.2 at the dendritic AISs between the species (Figure 7I). Therefore, we speculate that the similar AnkG- and Nav1.2-labeled lengths may be related to the comparable bpAP and fpAP speeds at dendritic AISs in both species (Figure 7J).

AnkG and Nav1.2 responded differently in rat and mouse neurons after AIS plasticity induction

We evaluated changes in AnkG and Nav1.2 staining length and location during AIS plasticity in neurons from SD rats and C57 mice. After 48 h of KCl treatment during long-term AIS plasticity, most AIS proteins (e.g., AnkG, NF-186, βIV spectrin, and Nav channels) move away from the soma (Grubb & Burrone, 2010a). In the present study, we focused on

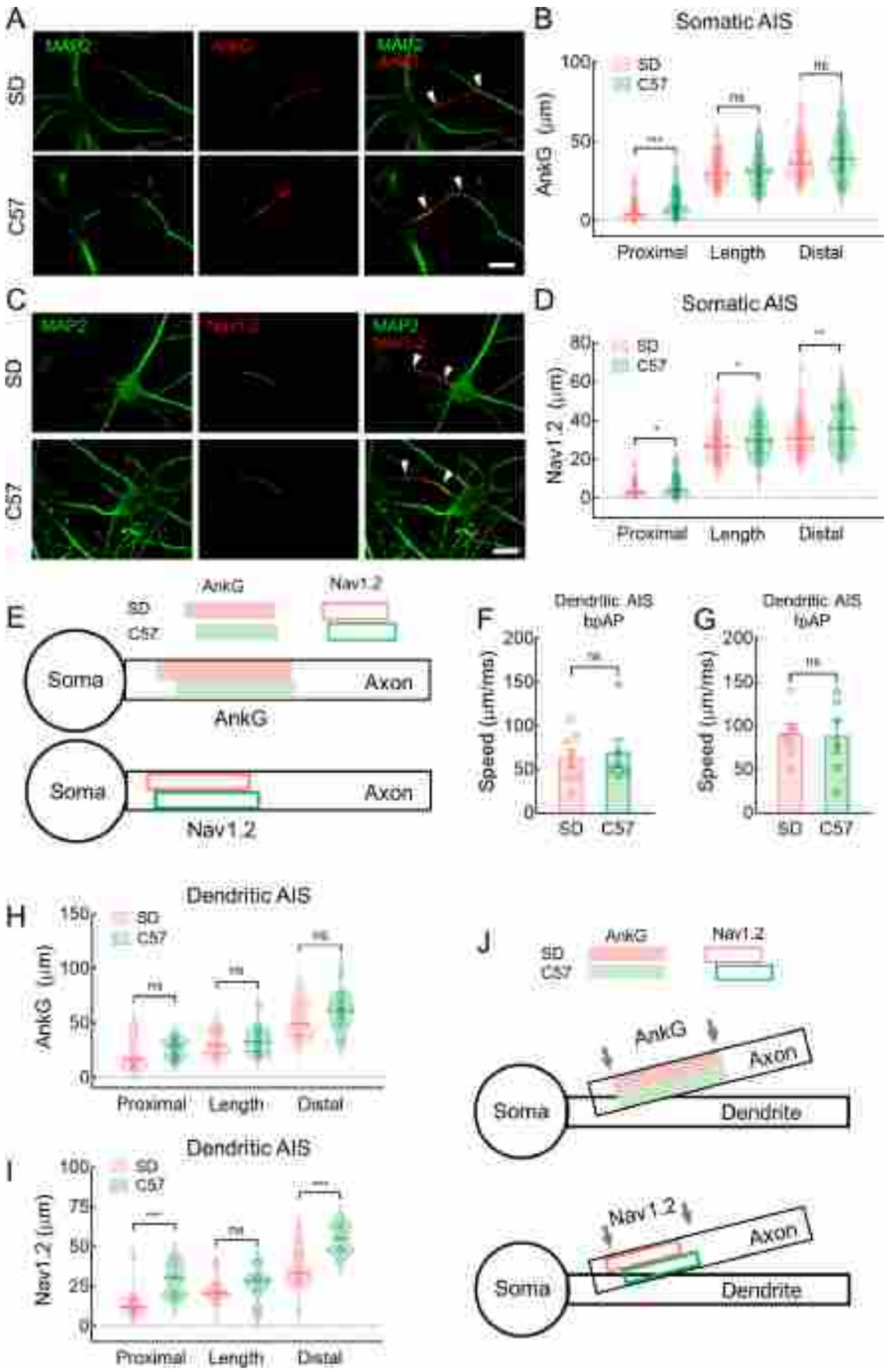
A
SD
C57
MAP2
AnkG
B
Somatic AIS
AnkG (μm)
SD
C57
Proximal
Length
Distal
C
Nav1.2
D
Somatic AIS
Nav1.2 (μm)
E
AnkG
Nav1.2
Soma
Axon
F
Dendritic AIS
fpAP
Speed (μm/ms)
G
Dendritic AIS
fpAP
H
Dendritic AIS
I
Dendritic AIS
J
Dendrite

Figure 7 Neurons from rats and mice exhibited very different AnkG and Nav1.2 patterns

A: Immunofluorescence images of AISs in neurons from rats and mice, as indicated by AnkG. Distance between two white arrowheads represents AIS length (Scale bars: 20 μm). B: In somatic AIS neurons in mice (green), AIS position was significantly distal compared to that in rats (pink), while AIS length was similar. Proximal end of AIS in rat neurons (6.44±0.50 μm, *n*=129) was significantly nearer soma than in mouse neurons (10.28±0.80 μm, *n*=79), ***: *P*<0.001. Length of AIS in rat neurons (31.36±0.76 μm, *n*=129) was similar to that in mouse neurons (30.62±1.15 μm, *n*=79), ns: *P*>0.05. Distal end of AIS in rat neurons (37.80±0.94 μm, *n*=129) was similar to that in mouse neurons (40.9±1.55 μm, *n*=79), ns: *P*>0.05. C: Immunofluorescence images of Nav1.2 in neurons from rats and mice. Distance between two white arrowheads represents Nav1.2 length (Scale bars: 20 μm). D: In somatic AIS neurons in mice (green), Nav1.2 length was longer than that in rats (pink), and proximal end location was similar. Proximal end of Nav1.2 in rat neurons (4.45±0.36 μm, *n*=105) was nearer soma than that in mouse neurons (6.25±0.66 μm, *n*=57), *: *P*<0.05. Length of Nav1.2 in rat neurons (27.41±0.76 μm, *n*=105) was significantly shorter than that in mouse neurons (30.04±1.11 μm, *n*=57), *: *P*<0.05. Distal end of Nav1.2 in rat neurons (31.87±0.85 μm, *n*=105) was significantly more proximal to soma than that in mouse neurons (36.31±1.38 μm, *n*=57), **: *P*<0.01. E: Schematic of AnkG and Nav1.2 position in somatic AIS neurons in rats and mice. Rat AnkG, pink filled box; mouse AnkG, green filled box; rat Nav1.2, pink box; mouse Nav1.2, green box. F: In dendritic AISs, bpAP speed at AIS in rat neurons (pink circles, 62.32±10.16 μm/ms, *n*=8) was comparable to that in mouse neurons (green circles, 68.63±16.14 μm/ms, *n*=6), ns: *P*>0.05. G: In dendritic AISs, fpAP speed at somatic AISs (pink circles, 90.30±12.23 μm/ms, *n*=6) was similar than that at dendritic AISs (green circles, 87.27±18.37 μm/ms, *n*=6), ns: *P*>0.05. H: In dendritic AIS neurons in mice (green), AIS location and length were similar to that in rats (pink). Dendritic AIS neurons in rats and mice exhibited similar AIS proximal end (20.82±3.05 μm, *n*=20; 26.36±1.78 μm, *n*=22, respectively, ns: *P*>0.05), AIS length (31.59±2.47 μm, *n*=20; 33.45±2.35 μm, *n*=22, respectively, ns: *P*>0.05), and AIS distal end (52.41±3.57 μm, *n*=20; 59.81±3.18 μm, *n*=22, respectively, ns: *P*>0.05). I: In dendritic AIS neurons in mice (green), Nav1.2 length was similar, while Nav1.2 was significantly distal compared to that in rats (pink). Proximal end of Nav1.2 in rat neurons (13.40±1.43 μm, *n*=27) was significantly nearer the soma than that in mouse neurons (28.54±2.78 μm, *n*=11), ***: *P*<0.001. Length of Nav1.2 in rat neurons (22.65±1.57 μm, *n*=27) was similar to that in mouse neurons (26.20±3.11 μm, *n*=11), ns: *P*>0.05. Distal end of Nav1.2 in rat neurons (36.06±2.26 μm, *n*=27) was significantly more proximal to soma than that in mouse neurons (54.74±2.54 μm, *n*=11), ***: *P*<0.001. J: Schematic of AnkG and Nav1.2 positions in dendritic AIS neurons in rats and mice. Rat AnkG, pink filled box; mouse AnkG, green filled box; rat Nav1.2, pink box; mouse Nav1.2, green box. Error bars represent *SEM*; two-tailed unpaired *t*-test was employed in B, D, F−I.

differences in neurons from rats and mice during AIS plasticity, especially short-term plasticity. A recent study reported that high glucose levels can alter the AIS position in mice with type 2 diabetes (Yermakov et al., 2018). We observed significant changes in AIS location/length after treating neurons with a high concentration of glucose for 3 h. Therefore, rather than 48 h of KCl treatment, we induced short-term AIS plasticity by exposing rat and mouse hippocampal neurons to high concentrations of glucose (20 mmol/L) for 3 h, then examined changes in AnkG and Nav1.2 staining length and location (Figure 8A, B) at the AIS. Overall, rat neurons treated with 20 mmol/L glucose for 3 h showed a significant distal shift in the AnkG-labeled proximal end (6.47±0.41 μm and 9.85±0.59 μm, respectively, ***: *P*<0.001) and significantly shortened AnkG-labeled length (31.98±0.74 μm and 28.21±0.89 μm, respectively, **: *P*<0.01). The AnkG-labeled distal end was similar in the glucose-treated and untreated groups (38.45±0.84 μm and 38.05±1.14 μm, respectively, ns: *P*>0.05) (Figure 8C, E). In addition, changes in Nav1.2-labeled length/location exhibited a comparable pattern to that of AnkG (Figure 8D, E).

However, in mouse neurons, the AnkG pattern shifted in the opposite direction after 3 h of 20 mmol/L glucose treatment. Specifically, compared with the untreated neurons, the glucose-treated neurons exhibited no distal shift in the AnkG-labeled proximal end (10.14±0.34 μm and 9.93±0.69 μm, respectively, ns: *P*>0.05) but showed a significantly shortened AnkG-labeled length (30.21±1.09 μm and 35.84±1.30 μm, respectively, **: *P*<0.01) due to a significant proximal shift in the AnkG-labeled distal end (40.34±1.24 μm and 45.77±1.46 μm, respectively, **: *P*<0.01) (Figure 8F, H). We also observed different changes in the length/location of Nav1.2 staining in the glucose-treated mouse neurons compared to the rat neurons. After 3 h of treatment with 20 mmol/L glucose, the proximal end of Nav1.2 staining exhibited a significant distal shift (6.18±0.48 μm and 9.66±0.83 μm, respectively, ***: *P*<0.001), but the distal end of Nav1.2 staining exhibited little change (length: 28.61±1.14 μm and 26.91±1.30 μm, respectively, ns: *P*>0.05; distal end: 34.79±1.24 μm and 36.57±1.52 μm, respectively, ns: *P*>0.05) (Figure 8G, H).

Consistent with AP propagation speed, neither bpAP nor fpAP speed changed at the dendritic AISs after 48 h of KCl treatment (Figure 5G, H). After inducing AIS plasticity by exposure to 20 mmol/L glucose for 3 h, only a distal shift in Nav1.2 localization was observed (Supplementary Figure S3B); neither the length of Nav1.2 staining nor the location and length of AnkG staining changed in the rat neurons (Supplementary Figure S3A–C). In the mouse neurons, no detectable changes in AnkG or Nav1.2 patterns were observed (Supplementary Figure S3D–F).

DISCUSSION

Electrode-based patch-clamp recordings are considered the "gold standard" for elucidating fluctuations in plasma membrane potential. However, the size of the pipette inhibits multi-site recordings at the tiny regions of the AIS and proximal axon. Furthermore, the axon is fragile (Ø=0.1–1.0 μm in axon and 1.0–2.5 μm in AIS), making it difficult to establish whole-cell recordings (Hu & Shu, 2012; Shu et al., 2006). Advanced axon-bleb recordings can only provide membrane potential details of a single site in the axon, which is insufficient to resolve the AP initiation site and calculate AP propagation speed at the AIS (Hu & Shu, 2012; Shu et al., 2006). High-density microelectrode arrays (HD-MEA) have been employed to resolve AP propagation at specific AISs

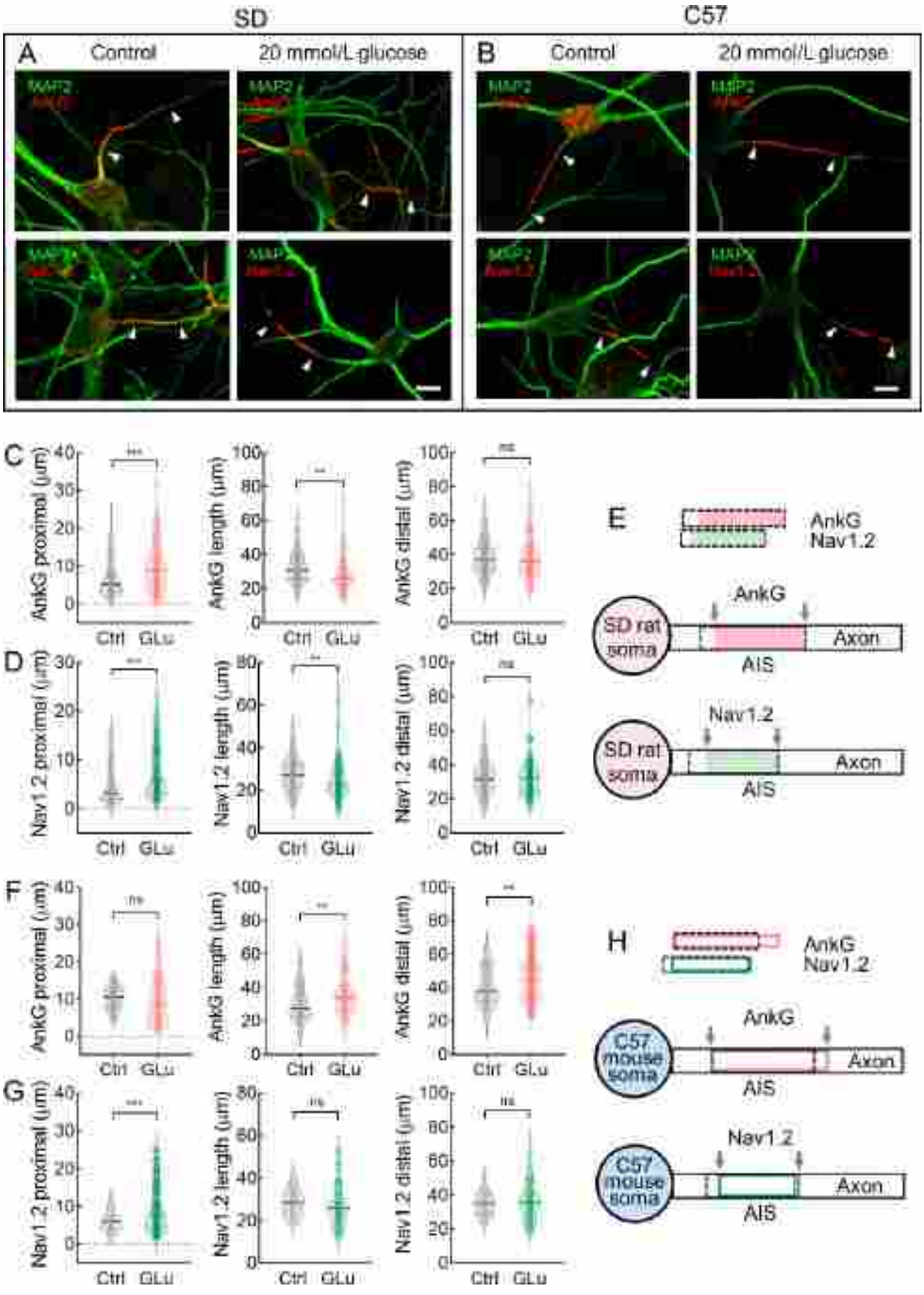
SD
C57
A
Control
20 mmol/L glucose
B
Control
20 mmol/L glucose
MAP2
Nav1.2
C
AnkG proximal (μm)
AnkG length (μm)
AnkG distal (μm)
Ctrl
GLu
D
Nav1.2 proximal (μm)
Nav1.2 length (μm)
Nav1.2 distal (μm)
E
AnkG
Nav1.2
SD rat soma
Axon
AIS
F
G
H
C57 mouse soma

Figure 8 AnkG and Nav1.2 length/location were differentially altered during AIS plasticity in somatic AIS neurons

A: Immunofluorescence images of AIS (upper) and Nav1.2 (under) in neurons from control rats (left) and 3 h 20 mmol/L glucose-treated rats (right). White arrowheads represent proximal and distal ends of AIS/Nav1.2 (Scale bars: 10 μm). B: Immunofluorescence images of AIS (upper) and Nav1.2 (under) in neurons from control mice (left) and 3 h 20 mmol/L glucose-treated mice (right). White arrowheads represent proximal and distal ends of AIS/Nav1.2 (Scale bars: 10 μm). C: In somatic AIS neurons in rats, compared with control group (gray), AIS location showed significant distal shift and shorter length in 3 h 20 mmol/L glucose-treated group (pink). Left, proximal end of AIS in 20 mmol/L glucose-treated group (9.85±0.59 μm, n=109) was significantly further from soma than that in control group (6.47±0.41 μm, n=126), ***: P<0.001. Middle, AIS length in 20 mmol/L glucose-treated group (28.21±0.89 μm, n=109) was significantly shorter than that in control group (31.98±0.74 μm, n=126), **: P<0.01. Right, distal end of AIS in 20 mmol/L glucose-treated group (38.05±1.14 μm, n=109) was similar to that in control group (38.45±0.84 μm, n=126), ns: P>0.05. D: In somatic AIS neurons in rats, compared with control group (gray), Nav1.2 location showed significant distal shift and shorter length in 3 h 20 mmol/L glucose-treated group (green). Left, proximal end of Nav1.2 in 20 mmol/L glucose-treated group (7.54±0.42 μm, n=150) was significantly further from soma than that in control group (4.41±0.34 μm, n=114), ***: P<0.001. Middle, Nav1.2 length in 20 mmol/L glucose-treated group (24.42±0.66 μm, n=150) was significantly shorter than that in control group (27.37±0.70 μm, n=114), **: P<0.01. Right, distal end of Nav1.2 in 20 mmol/L glucose-treated group (31.96±0.81 μm, n=150) was similar to that in control group (31.77±0.84 μm, n=114), ns: P>0.05. E: Schematic of AnkG and Nav1.2 position in rats. AnkG, pink filled box, Nav1.2, green filled box. F: In somatic AIS neurons in mice, compared with control group (gray), AIS length was longer in 3 h 20 mmol/L glucose-treated group (pink), while AIS location was similar. Left, proximal end of AIS in 20 mmol/L glucose-treated group (9.93±0.69 μm, n=81) was similar to that in control group (10.14±0.34 μm, n=77), ns: P>0.05. Middle, AIS length in 20 mmol/L glucose-treated group (35.84±1.30 μm, n=81) was significantly longer than that in control group (30.21±1.09 μm, n=77), **: P<0.01. Right, distal end of AIS in 20 mmol/L glucose-treated group (45.77±1.46 μm, n=81) showed significant distal shift compared with control group (40.34±1.24 μm, n=77), **: P<0.01. G: In somatic AIS neurons in mice, compared with control group (gray), Nav1.2 location showed significant distal shift in 3 h 20 mmol/L glucose-treated group (green), while Nav1.2 length was similar. Left, proximal end of Nav1.2 in 20 mmol/L glucose-treated group (9.66±0.83 μm, n=57) was significantly further from soma than that in control group (6.18±0.48 μm, n=30), ***: P<0.001. Middle, Nav1.2 length in 20 mmol/L glucose-treated group (26.91±1.30 μm, n=57) was similar to that in control group (28.61±1.14 μm, n=30), ns: P>0.05. Right, distal end of Nav1.2 in 20 mmol/L glucose-treated group (36.57±1.52 μm, n=57) was similar to that in control group (34.79±1.24 μm, n=30), ns: P>0.05. H: Schematic of AnkG and Nav1.2 position in mice. AnkG, pink box, Nav1.2, green box. Error bars represent *SEM*; two-tailed unpaired *t*-test was employed in C, D, F, G.

with higher spatiotemporal resolution (Abbott et al., 2020; Bakkum et al., 2013; Emmenegger et al., 2019). While these electrode-based techniques have advanced our knowledge of AIS electrophysiology, they suffer from high cell invasiveness, poor spatial resolution, and high labor costs.

In contrast to the above-mentioned techniques, optical voltage imaging can simultaneously measure changes in membrane potential from different sites on one neurite to large neural populations with high spatial resolution due to higher sampling density compared to electrode-based techniques (Peng et al., 2017; Xu et al., 2017). In recent years, voltage imaging has emerged as a powerful technique to clarify AP propagation details along the axon, such as the AIS (Foust et al., 2010; Hochbaum et al., 2014; Popovic et al., 2011; Sabater et al., 2021). Due to technical limitations in measuring AP speed at the AIS and proximal axon adjacent to the soma, several questions have remained unanswered, such as whether AIS morphology influences AP propagation and whether fpAP and bpAP speeds are similar at the AIS. Taking advantage of voltage imaging technology, we examined AP generation and propagation in hippocampal neurons of SD rats and C57 mice. We found that AP propagation speed varied along the proximal axon, and generally, bpAP speed was lower than fpAP speed at the AISs (Figure 2F).

We simultaneously recorded electrical and optical signals in the soma. Somatic AP comparison of GEVI recordings with whole-cell patch-clamp recordings showed that APs were accurately and reliably captured (Figure 1C). Moreover, calculation of bpAP propagation at the dendrites produced similar results to previous patch-clamp recordings (Larkum et al., 2001; Nevian et al., 2007) and functional imaging (Antic, 2003; Kampa & Stuart, 2006) of apical/basal dendrites of rats and mice (Supplementary Figure S4). As mentioned above, *in situ* interrogation of AP propagation at the AIS via multielectrode intracellular patch-clamp recording has remained a technical challenge (Yang et al., 2019). Thus, we were unable to validate our method directly using electrode-based "gold-standard techniques" at the AIS. In comparison, fluctuations in bpAP amplitude and propagation speed have been well studied using traditional dendritic electrophysiology in rat Purkinje cells and layer 5 pyramidal neurons (Larkum et al., 2001; Nevian et al., 2007; Vetter et al., 2001). Although dendritic morphologies, molecular structures, and intercellular connections differ in cultured hippocampal neurons and neurons in brain slices, we compared dendritic AP propagation using our voltage imaging method to that using multielectrode patch-clamp recording (Emmenegger et al., 2019; Liu & Miller, 2020; Xu et al., 2017). Similar results were obtained, implying that our optical method provided decent temporal accuracy after interpolation and may support more informative monitoring of voltage changes via multi-site imaging (Emmenegger et al., 2019; Liu & Miller, 2020; Xu et al., 2017).

Our results also showed that, in the somatic AIS neurons, bpAP speed was not influenced by AIS location or length (Figure 2G, H). However, fpAP speed was lower at the distal AISs and shorter AISs (Figure 2I, J). Low-threshold Nav1.6 channels accumulate at the distal AIS and play an important role in AP initiation, whereas high-threshold Nav1.2 channels preferentially accumulate at the proximal AIS and play an important role in bpAP propagation (Hu et al., 2009). Our data showed that the AP initiation site was located far from the

soma at longer AISs or distally located AISs (Supplementary Figure S5A, B). Compared with fpAPs, bpAPs pass through longer Nav1.2 channels during backpropagation. Therefore, during propagation to the axon terminal, fpAPs are transmitted by a limited number of Nav1.2 channels and high-density Nav1.6 channels, as well as other ion channels, which may make fpAPs more susceptible to changes in AIS length/location. We speculate that during AIS plasticity, the distribution (length/location/density) of ion channels in the AIS will change with AIS location/length. Thus, somatic AIS neurons are more likely to regulate homeostasis through AIS plasticity after exposure to external stimuli, and AIS plasticity exerts a greater effect on fpAPs.

Our results also indicated that bpAP speed at dendritic AISs was approximately 60% of that at the somatic AISs in the SD rat and C57 mouse neurons (Figure 4C, 6B). According to the simulations, AP speed was lower in the dendritic AISs because their diameters were thicker than those of the somatic AISs (Figure 4D, E). Compared to the speed recorded at the somatic AISs, AP speed at the dendritic AISs was less sensitive to external stimulation (Figure 5A, B). On the other hand, when we used 20 mmol/L glucose to induce AIS plasticity, the length/location of AnkG and Nav1.2 staining at the dendritic AISs changed very little. One possible explanation is that the dendritic AIS neurons adapted to external stimuli through a different mechanism than the somatic AIS neurons, and the thick dendrite between the AIS and soma may function as a buffer zone during external stimulation.

After inducing AIS plasticity by administering glucose to rat and mouse neurons, we observed different changes in the distributions of AnkG and Nav1.2 in the somatic AIS neurons. In the rat neurons, during AIS plasticity, the proximal ends of both AnkG and Nav1.2 staining shifted distally, and shorter AnkG/Nav1.2 staining lengths were observed (Figure 8C–E). In the mouse neurons, during AIS plasticity, the proximal end of the AnkG-labeled AISs did not change but an increase in length and a distal shift at the distal end were observed; the proximal end of Nav1.2 staining also exhibited a distal shift, but with no change in length (Figure 8F–H). These results suggest that AISs in rat and mouse hippocampal neurons undergo different changes in AIS plasticity when subjected to external stimuli. This AIS plasticity, combined with synaptic plasticity, may play an important role in learning and memory. For example, previous studies have reported that mice use different strategies for learning spatial information than rats. In the Morris water maze, a spatial memory task in which spatial cues are used to lead rodents through a circular pool to a hidden platform, rats generally perform better than mice (Frick et al., 2000; Whishaw, 1995). On the other hand, mice use simpler strategies than rats in the platform location test (Whishaw et al., 2001).

The distinct AIS features reported in this study may also be related to differences in functional and neurological disorders between rats and mice. For instance, fundamental species differences exist between rats and mice in the distribution of the serotonin (5-HT) receptor subtype 5-HT6 (Hirst et al., 2003). High levels of leucine rich repeat kinase 2 (LRRK2), which is linked to Parkinson's disease, in the dopaminergic cell body region of the substantia nigra pars compacta are reported in mice but not in rats, which may affect studies on neurodegenerative diseases (Klein & Westenberger, 2012). In particular, important and fundamental differences in neurogenesis in regions such as the hippocampus have been observed between rats and mice (Lazarov & Hollands, 2016). Snyder et al. (2009) found that the rate of hippocampal neurogenesis is much higher in rats than in mice, and that hippocampal cells mature two weeks earlier, are more likely to escape cell death, and are 10 times more likely to be activated during learning in rats than in mice, thus revealing substantial differences in neuronal plasticity between the two species.

In conclusion, our study revealed several differences in neuronal AISs in rats and mice and in the performance of AIS plasticity between the two species, suggesting that mice are not simply "little rats". Thus, comparing data from different species must carefully consider these and potentially other physiological and anatomical differences.

SUPPLEMENTARY DATA

Supplementary data to this article can be found online.

COMPETING INTERESTS

The authors declare that they have no competing interests.

AUTHORS' CONTRIBUTIONS

Z.Y.C., L.P., M.Z., Y.L., and M.T. performed all experiments and analyzed the data. Y.Z., P.Z., and L.T. conceptualized the study, performed analyses, and drafted the manuscript with input from all authors. All authors read and approved the final version of the manuscript.

ACKNOWLEDGMENTS

We thank the National Center for Protein Sciences at Peking University, Beijing, China, and the State Key Laboratory of Membrane Biology at Peking University, Beijing, China, for their assistance.

REFERENCES

Abbott J, Ye TY, Krenek K, Gertner RS, Ban S, Kim Y, et al. 2020. A nanoelectrode array for obtaining intracellular recordings from thousands of connected neurons. *Nature Biomedical Engineering*, **4**(2): 232−241.

Alle H, Geiger JRP. 2006. Combined analog and action potential coding in hippocampal mossy fibers. *Science*, **311**(5765): 1290−1293.

Antic SD. 2003. Action potentials in basal and oblique dendrites of rat neocortical pyramidal neurons. *The Journal of Physiology*, **550**(1): 35−50.

Atherton JF, Wokosin DL, Ramanathan S, Bevan MD. 2008. Autonomous initiation and propagation of action potentials in neurons of the subthalamic nucleus. *The Journal of Physiology*, **586**(23): 5679−5700.

Bakkum DJ, Frey U, Radivojevic M, Russell TL, Müller J, Fiscella M, et al. 2013. Tracking axonal action potential propagation on a high-density microelectrode array across hundreds of sites. *Nature Communications*, **4**: 2181.

Bando Y, Sakamoto M, Kim S, Ayzenshtat I, Yuste R. 2019. Comparative evaluation of genetically encoded voltage indicators. *Cell Reports*, **26**(3): 802−813.e4.

Bashir ZI, Collingridge GL. 1992. Synaptic plasticity: long-term potentiation in the hippocampus. *Current Opinion in Neurobiology*, **2**(3): 328−335.
Bender KJ, Trussell LO. 2012. The physiology of the axon initial segment. *Annual Review of Neuroscience*, **35**: 249−265.
Chen R, Tilley MR, Wei H, Zhou FW, Zhou FM, Ching S, et al. 2006. Abolished cocaine reward in mice with a cocaine-insensitive dopamine transporter. *Proceedings of the National Academy of Sciences of the United States of America*, **103**(24): 9333−9338.
Clark BD, Goldberg EM, Rudy B. 2009. Electrogenic tuning of the axon initial segment. *The Neuroscientist*, **15**(6): 651−668.
Cui J, Wang YF, Dong QP, Wu SM, Xiao XZ, Hu JY, et al. 2011. Morphine protects against intracellular amyloid toxicity by inducing estradiol release and upregulation of Hsp70. *Journal of Neuroscience*, **31**(45): 16227−16240.
Debanne D. 2004. Information processing in the axon. *Nature Reviews Neuroscience*, **5**(4): 304−316.
DRaDR A. 1922. SEMON, R. -The Mneme.
Emmenegger V, Obien MEJ, Franke F, Hierlemann A. 2019. Technologies to study action potential propagation with a focus on HD-MEAs. *Frontiers in Cellular Neuroscience*, **13**: 159.
Evans MD, Dumitrescu AS, Kruijssen DLH, Taylor SE, Grubb MS. 2015. Rapid modulation of axon initial segment length influences repetitive spike firing. *Cell Reports*, **13**(6): 1233−1245.
Foust A, Popovic M, Zecevic D, McCormick DA. 2010. Action potentials initiate in the axon initial segment and propagate through axon collaterals reliably in cerebellar purkinje neurons. *Journal of Neuroscience*, **30**(20): 6891−6902.
Frick KM, Stillner ET, Berger-Sweeney J. 2000. Mice are not little rats: species differences in a one-day water maze task. *Neuroreport*, **11**(16): 3461−3465.
Fried SI, Lasker ACW, Desai NJ, Eddington DK, Rizzo III JF. 2009. Axonal sodium-channel bands shape the response to electric stimulation in retinal ganglion cells. *Journal of Neurophysiology*, **101**(4): 1972−1987.
Golding NL, Mickus TJ, Katz Y, Kath WL, Spruston N. 2005. Factors mediating powerful voltage attenuation along CA1 pyramidal neuron dendrites. *The Journal of Physiology*, **568**(1): 69−82.
Goldstein SS, Rall W. 1974. Changes of action potential shape and velocity for changing core conductor geometry. *Biophysical Journal*, **14**(10): 731−757.
Grubb MS, Burrone J. 2010a. Activity-dependent relocation of the axon initial segment fine-tunes neuronal excitability. *Nature*, **465**(7301): 1070−1074.
Grubb MS, Burrone J. 2010b. Building and maintaining the axon initial segment. *Current Opinion in Neurobiology*, **20**(4): 481−488.
Grubb MS, Shu YS, Kuba H, Rasband MN, Wimmer VC, Bender KJ. 2011. Short-and long-term plasticity at the axon initial segment. *Journal of Neuroscience*, **31**(45): 16049−16055.
Harris KM, Stevens JK. 1989. Dendritic spines of CA 1 pyramidal cells in the rat hippocampus: serial electron microscopy with reference to their biophysical characteristics. *Journal of Neuroscience*, **9**(8): 2982−2997.
Hickman-Davis JM, Davis IC. 2006. Transgenic mice. *Paediatric Respiratory Reviews*, **7**(1): 49−53.
Hirst WD, Abrahamsen B, Blaney FE, Calver AR, Aloj L, Price GW, et al. 2003. Differences in the central nervous system distribution and pharmacology of the mouse 5-hydroxytryptamine-6 receptor compared with rat and human receptors investigated by radioligand binding, site-directed mutagenesis, and molecular modeling. *Molecular Pharmacology*, **64**(6): 1295−1308.
Hochbaum DR, Zhao YX, Farhi SL, Klapoetke N, Werley CA, Kapoor V, et al. 2014. All-optical electrophysiology in mammalian neurons using engineered microbial rhodopsins. *Nature Methods*, **11**(8): 825−833.
Hu WQ, Shu YS. 2012. Axonal bleb recording. *Neuroscience Bulletin*, **28**(4): 342−350.
Hu WQ, Tian CP, Li T, Yang MP, Hou H, Shu YS. 2009. Distinct contributions of Na(v)1.6 and Na(v)1.2 in action potential initiation and backpropagation. *Nature Neuroscience*, **12**(8): 996−1002.
Jarrard LE. 1993. On the role of the hippocampus in learning and memory in the rat. *Behavioral and Neural Biology*, **60**(1): 9−26.
Josselyn SA, Köhler S, Frankland PW. 2015. Finding the engram. *Nature Reviews Neuroscience*, **16**(9): 521−534.
Josselyn SA, Köhler S, Frankland PW. 2017. Heroes of the engram. *Journal of Neuroscience*, **37**(18): 4647−4657.
Kamal A, Biessels GJ, Urban IJA, Gispen WH. 1999. Hippocampal synaptic plasticity in streptozotocin-diabetic rats: impairment of long-term potentiation and facilitation of long-term depression. *Neuroscience*, **90**(3): 737−745.
Kampa BM, Stuart GJ. 2006. Calcium spikes in basal dendrites of layer 5 pyramidal neurons during action potential bursts. *Journal of Neuroscience*, **26**(28): 7424−7432.
Kiskinis E, Kralj JM, Zou P, Weinstein EN, Zhang HK, Tsioras K, et al. 2018. All-optical electrophysiology for high-throughput functional characterization of a human iPSC-derived motor neuron model of ALS. *Stem Cell Reports*, **10**(6): 1991−2004.
Klein C, Westenberger A. 2012. Genetics of parkinson's disease. *Cold Spring Harbor Perspectives in Medicine*, **2**(1): a008888.
Kole MHP, Letzkus JJ, Stuart GJ. 2007. Axon initial segment Kv1 channels control axonal action potential waveform and synaptic efficacy. *Neuron*, **55**(4): 633−647.
Kole MHP, Stuart GJ. 2012. Signal processing in the axon initial segment. *Neuron*, **73**(2): 235−247.
Kuba H, Ishii TM, Ohmori H. 2006. Axonal site of spike initiation enhances auditory coincidence detection. *Nature*, **444**(7122): 1069−1072.
Kuba H, Oichi Y, Ohmori H. 2010. Presynaptic activity regulates Na^+ channel distribution at the axon initial segment. *Nature*, **465**(7301): 1075−1078.
Kuba H, Yamada R, Ishiguro G, Adachi R. 2015. Redistribution of Kv1 and Kv7 enhances neuronal excitability during structural axon initial segment plasticity. *Nature Communications*, **6**: 8815.
Larkum ME, Zhu JJ, Sakmann B. 2001. Dendritic mechanisms underlying the coupling of the dendritic with the axonal action potential initiation zone of adult rat layer 5 pyramidal neurons. *The Journal of Physiology*, **533**(2): 447−466.
Lazarov O, Hollands C. 2016. Hippocampal neurogenesis: learning to remember. *Progress in Neurobiology*, **138–140**: 1–18.
Leterrier C. 2018. The axon initial segment: an updated viewpoint. *Journal of Neuroscience*, **38**(9): 2135−2145.
Liu P, Miller EW. 2020. Electrophysiology, unplugged: imaging membrane potential with fluorescent indicators. *Accounts of Chemical Research*, **53**(1): 11−19.
Lorincz A, Nusser Z. 2010. Molecular identity of dendritic voltage-gated sodium channels. *Science*, **328**(5980): 906−909.
Mainen ZF, Sejnowski TJ. 1998. Modeling active dendritic processes in pyramidal neurons. *In*: Koch C, Segev I. Methods in Neuronal Modeling.

Cambridge: MIT Press, 171–210.
Megías M, Emri Z, Freund TF, Gulyás AI. 2001. Total number and distribution of inhibitory and excitatory synapses on hippocampal CA1 pyramidal cells. *Neuroscience*, **102**(3): 527−540.
Morris RG. 1989. Synaptic plasticity and learning: selective impairment of learning rats and blockade of long-term potentiation in vivo by the N-methyl-D-aspartate receptor antagonist AP5. *Journal of Neuroscience*, **9**(9): 3040−3057.
Morris RG, Davis S, Butcher SP. 1990. Hippocampal synaptic plasticity and NMDA receptors: a role in information storage?. *Philosophical Transactions of the Royal Society B:Biological Sciences*, **329**(1253): 187−204.
Muir J, Kittler JT. 2014. Plasticity of $GABA_A$ receptor diffusion dynamics at the axon initial segment. *Frontiers in Cellular Neuroscience*, **8**: 151.
Nevian T, Larkum ME, Polsky A, Schiller J. 2007. Properties of basal dendrites of layer 5 pyramidal neurons: a direct patch-clamp recording study. *Nature Neuroscience*, **10**(2): 206−214.
Nolan MF, Malleret G, Dudman JT, Buhl DL, Santoro B, Gibbs E, et al. 2004. A behavioral role for dendritic integration: HCN1 channels constrain spatial memory and plasticity at inputs to distal dendrites of CA1 pyramidal neurons. *Cell*, **119**(5): 719−732.
Peng LX, Xu YX, Zou P. 2017. Genetically-encoded voltage indicators. *Chinese Chemical Letters*, **28**(10): 1925−1928.
Picciotto MR, Wickman K. 1998. Using knockout and transgenic mice to study neurophysiology and behavior. *Physiological Reviews*, **78**(4): 1131−1163.
Poirazi P, Brannon T, Mel BW. 2003. Arithmetic of subthreshold synaptic summation in a model CA1 pyramidal cell. *Neuron*, **37**(6): 977−987.
Popovic MA, Foust AJ, McCormick DA, Zecevic D. 2011. The spatio-temporal characteristics of action potential initiation in layer 5 pyramidal neurons: a voltage imaging study. *The Journal of Physiology*, **589**(17): 4167−4187.
Rama S, Zbili M, Debanne D. 2018. Signal propagation along the axon. *Current Opinion in Neurobiology*, **51**: 37−44.
Rasband MN. 2010. The axon initial segment and the maintenance of neuronal polarity. *Nature Reviews Neuroscience*, **11**(8): 552−562.
Rocha-Martins M, Cavalheiro GR, Matos-Rodrigues GE, Martins RAP. 2015. From Gene Targeting to Genome Editing: transgenic animals applications and beyond. *Anais da Academic Brasileira de Ciencias*, **87**(2 Suppl): 1323–1348.
Routh BN, Johnston D, Harris K, Chitwood RA. 2009. Anatomical and electrophysiological comparison of CA1 pyramidal neurons of the rat and mouse. *Journal of Neurophysiology*, **102**(4): 2288−2302.
Sabater VG, Rigby M, Burrone J. 2021. Voltage-gated potassium channels ensure action potential shape fidelity in distal axons. *The Journal of Neuroscience*, **41**(25): 5372−5385.
Saraga F, Wu CP, Zhang L, Skinner FK. 2003. Active dendrites and spike propagation in multicompartment models of oriens‐lacunosum/moleculare hippocampal interneurons. *The Journal of Physiology*, **552**(3): 673−689.
Schmidt-Hieber C, Jonas P, Bischofberger J. 2008. Action potential initiation and propagation in hippocampal mossy fibre axons. *The Journal of Physiology*, **586**(7): 1849−1857.
Shu YS, Hasenstaub A, Duque A, Yu YG, McCormick DA. 2006. Modulation of intracortical synaptic potentials by presynaptic somatic membrane potential. *Nature*, **441**(7094): 761−765.
Snyder JS, Choe JS, Clifford MA, Jeurling SI, Hurley P, Brown A, et al. 2009. Adult-born hippocampal neurons are more numerous, faster maturing, and more involved in behavior in rats than in mice. *Journal of Neuroscience*, **29**(46): 14484−14495.
Sun XQ, Wu Y, Gu MX, Liu Z, Ma YL, Li J, et al. 2014. Selective filtering defect at the axon initial segment in Alzheimer's disease mouse models. *Proceedings of the National Academy of Sciences of the United States of America*, **111**(39): 14271−14276.
Thome C, Kelly T, Yanez A, Schultz C, Engelhardt M, Cambridge SB, et al. 2014. Axon-carrying dendrites convey privileged synaptic input in hippocampal neurons. *Neuron*, **83**(6): 1418−1430.
Tonegawa S, Liu X, Ramirez S, Redondo R. 2015. Memory engram cells have come of age. *Neuron*, **87**(5): 918−931.
Triarhou LC. 2014. Axons emanating from dendrites: phylogenetic repercussions with Cajalian hues. *Frontiers in Neuroanatomy*, **8**: 133.
Vetter P, Roth A, Häusser M. 2001. Propagation of action potentials in dendrites depends on dendritic morphology. *Journal of Neurophysiology*, **85**(2): 926−937.
Voronin LL. 1993. On the quantal analysis of hippocampal long-term potentiation and related phenomena of synaptic plasticity. *Neuroscience*, **56**(2): 275−304.
Wang LF, Wang HT, Yu LC, Chen Y. 2011. Role of axonal sodium-channel band in neuronal excitability. *Physical Review E*, **84**(5): 052901.
Whishaw IQ. 1995. A comparison of rats and mice in a swimming pool place task and matching to place task: some surprising differences. *Physiology & Behavior*, **58**(4): 687−693.
Whishaw IQ, Metz GAS, Kolb B, Pellis SM. 2001. Accelerated nervous system development contributes to behavioral efficiency in the laboratory mouse: a behavioral review and theoretical proposal. *Developmental Psychobiology*, **39**(3): 151−170.
Wyass JM, Van Groen T. 1992. Connections between the retrosplenial cortex and the hippocampal formation in the rat: a review. *Hippocampus*, **2**(1): 1−11.
Xu YX, Zou P, Cohen AE. 2017. Voltage imaging with genetically encoded indicators. *Current Opinion in Chemical Biology*, **39**: 1−10.
Yamada R, Kuba H. 2016. Structural and functional plasticity at the axon initial segment. *Frontiers in Cellular Neuroscience*, **10**: 250.
Yang J, Xiao YJ, Li L, He QS, Li M, Shu YS. 2019. Biophysical properties of somatic and axonal voltage-gated sodium channels in midbrain dopaminergic neurons. *Frontiers in Cellular Neuroscience*, **13**: 317.
Yermakov LM, Drouet DE, Griggs RB, Elased KM, Susuki K. 2018. Type 2 diabetes leads to axon initial segment shortening in *db/db* mice. *Frontiers in Cellular Neuroscience*, **12**: 146.

Supplementary Materials

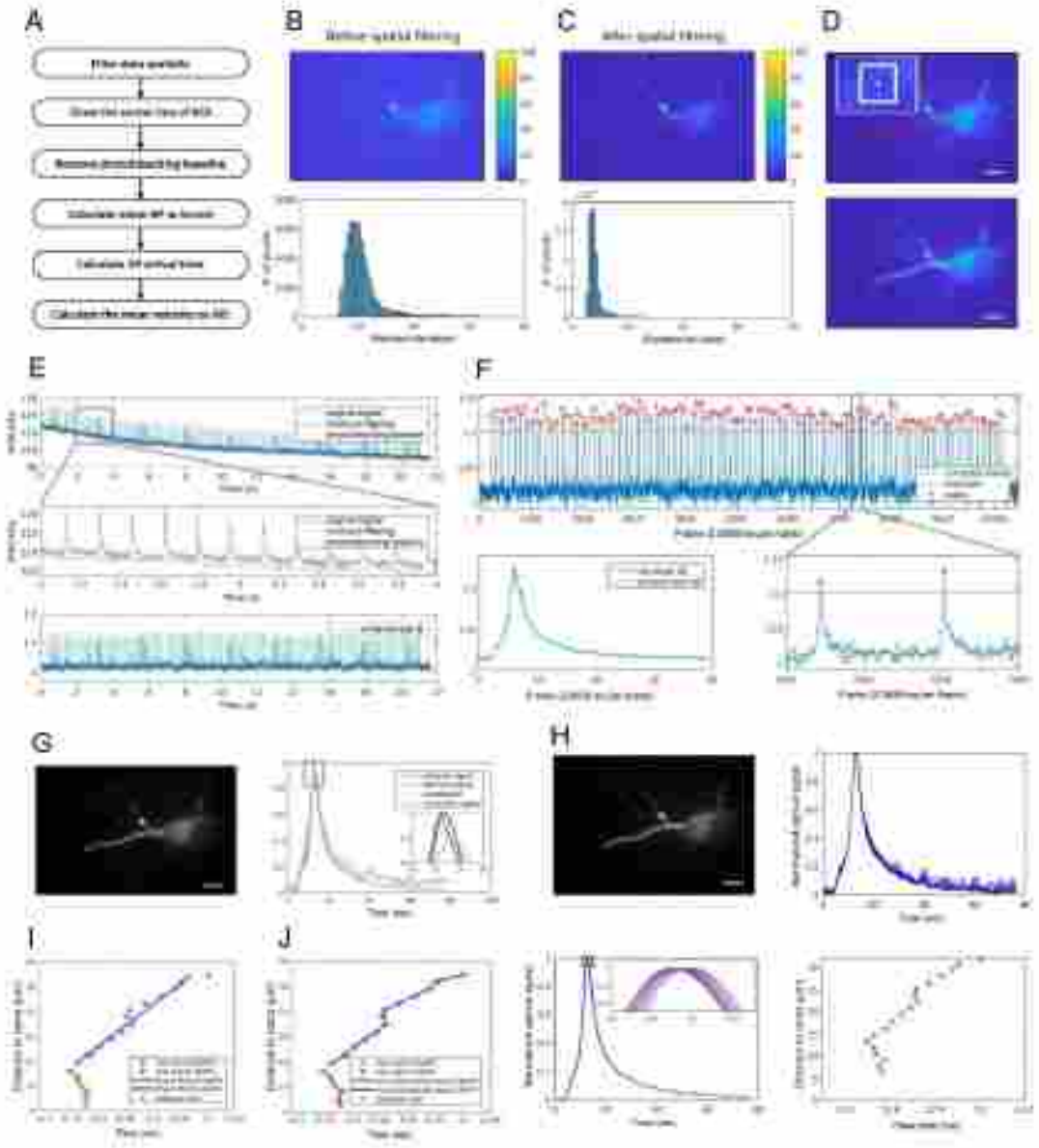

Supplementary Figure S1 Process of calculating propagation speed from raw data

Data processing method was used to extract AP speed from raw voltage imaging data, including: spatially filtering data, drawing centerline of ROI, removing photobleaching baseline, calculating mean AP as kernel, calculating AP arrival time, and calculating mean speed on AIS.

A. Flow chart of data processing method.

B. Upper image is raw image of a neuron, where value of each pixel is the standard deviation of intensity throughout voltage imaging. Lower image is the standard deviation histogram of the pixels in the upper image.

C. Upper image is an image of a neuron after spatial filtering, where value of each pixel is

the standard deviation of intensity throughout voltage imaging. Lower image is the standard deviation histogram of the pixels in the upper image.

D. Upper image is intensity image of a neuron. Red line is the centerline of an axon drawn by the user. Inner image shows how ROI is delineated: size of white square is 5×5; window slides along red line, with center white point located on the red line; region slid by the window is the ROI. White line in lower image is ROI (Scale bar: 10 μm).

E. Removal of photobleaching. Upper, blue line is the original (raw) signal of the ROI. Red line is the minimum filtering result of the blue line. Yellow line is the baseline of photobleaching calculated via a mean filter applied to the red line. Middle, larger image of gray square in the upper image. Lower, corrected signal of ROI (ΔF/F) calculated by original signal (blue) divided by photobleaching baseline (yellow).

F. Mean AP calculation. Upper, peaks of each APs. Blue signal is corrected signal after removing the photobleaching baseline. Red line is a manual threshold; APs whose maximum voltage was higher than the threshold were considered normal and used to calculate mean AP. Red stars are peaks of each AP. Lower right image is larger image of the gray rectangle. Lower left image is mean AP, i.e., mean of all selected APs aligned with AP peaks.

G. Correct signals on each segment. Left, region circled by white line is ROI. Red and blue points are sampled locations in the axon. Green region is one segment with red-point center. Right, blue AP trace is the original signal, i.e., mean intensity of green region in left image. Red AP trace is interpolated from blue trace by cubic spline interpolation. Yellow AP trace is correlation function between blue and red traces. Purple AP trace is corrected signal, i.e., final result of this step.

H. Time-aligned corrected AP traces from different locations for a cell. Upper left, axon is circled with a white line. Points gradually changing from red (close to soma) and blue (far from soma), are in different locations in the axon. Upper right, normalized raw optical signals at each location. Lower left, corrected mean APs at each location. Inner figure is magnified gray rectangle, showing AP peaks. Lower right, peak time of APs at each location. Color of four images is consistent.

I. Mean speed calculation. Red and blue stars are peak times of bpAPs and fpAPs, respectively. Red and blue lines are linear fitting lines. Slopes of red and blue lines are mean speeds of bpAP and fpAP, respectively. Green point is initiation site.

J. Instantaneous speed calculation. Red and blue stars are peak times of bpAPs and fpAPs, respectively. Least-squares curve fitting was used to calculate red and blue curves with linear constraints. Slope of curves at each location is instantaneous speed at each position. Green point is initiation site.

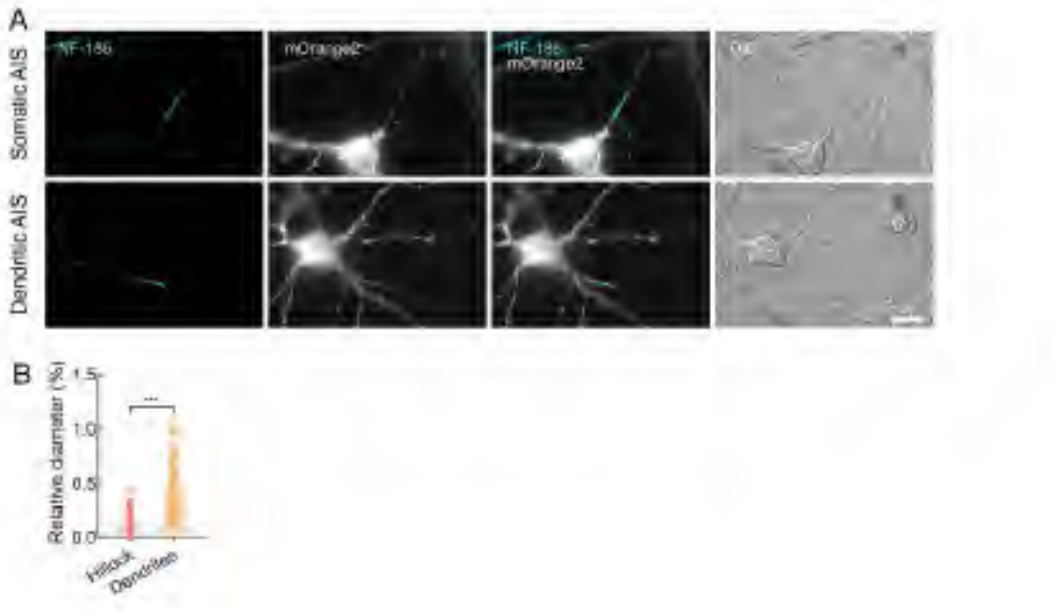

Supplementary Figure S2 Representative images of distal-shifted AISs after KCl treatment in somatic AIS and dendritic AIS neurons.

A. Representative images of cultured wild-type rat hippocampal neurons (DIV12) after 48 h of treatment with 15 mmol/L KCl. All neurons were transfected at DIV7 with QuasAr2-mOrange2 plasmid. Selected neurons (white) and their AISs (blue) are indicated by fluorescence of mOrange2 and axonal marker NF-186, respectively. Corresponding DIC images correspond to neurons in left column (scale bars: 20 μm).

B. Relative diameter of dendrites (n=39 was much thicker than that of hillock (n=62), ***: P<0.001.

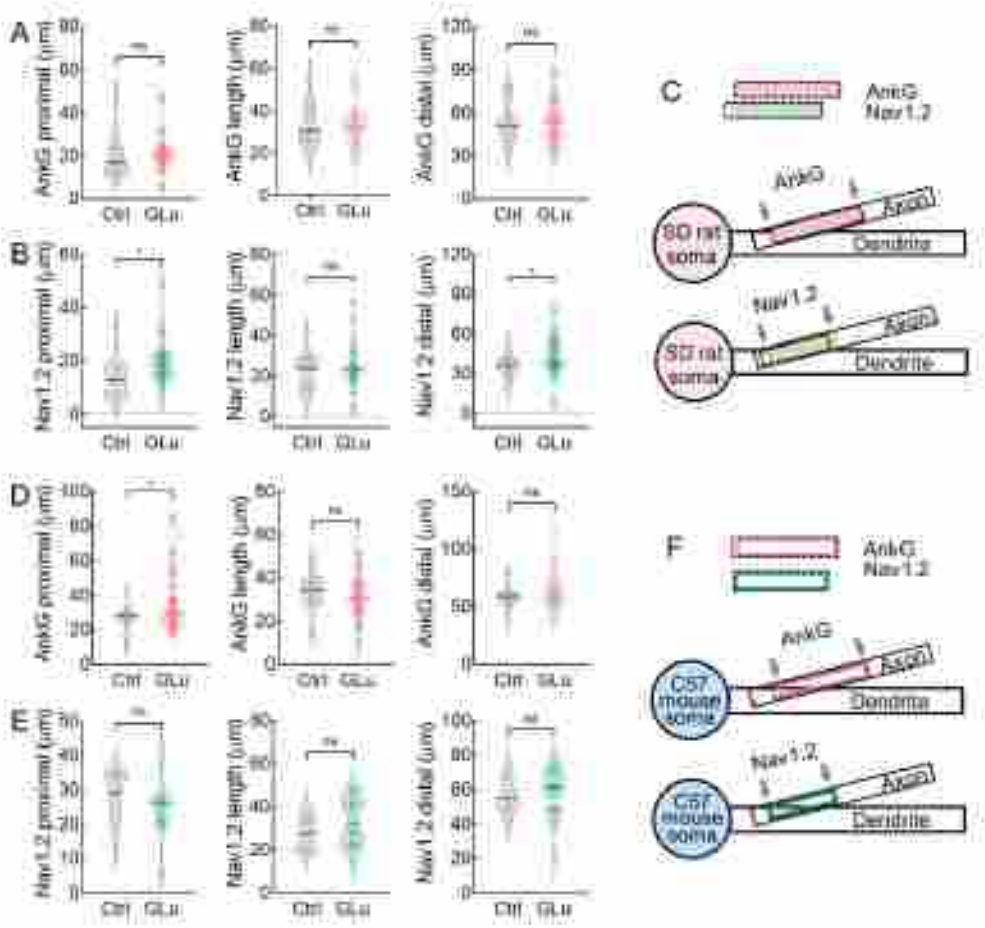

Supplementary Figure S3 AnkG and Nav1.2 length/location in dendritic AISs exhibited little change after treatment with 20 mmol/L glucose

A. In dendritic AIS neurons in rats, compared with control group (gray), both AIS location and length were similar to 3 h 20 mmol/L glucose-treated group (pink). Left, proximal end of AIS in 20 mmol/L glucose-treated group (20.65±1.51 μm, n=24) was similar to that in control group (20.13±2.18 μm, n=23), ns: P>0.05. Middle, AIS length in 20 mmol/L glucose-treated group (32.78±2.0 μm, n=24) was similar to that in control group (32.17±1.89 μm, n=23), ns: P>0.05. Right, distal end of AIS in 20 mmol/L glucose-treated group (53.43±2.81 μm, n=24) was similar to that in control group (52.30±2.88 μm, n=23), ns: P>0.05.

B. In dendritic AIS neurons in rats, compared with control group (gray), Nav1.2 location showed significant distal shift but similar length in 3 h 20 mmol/L glucose-treated group (green). Left, proximal end of Nav1.2 in 20 mmol/L glucose-treated group (18.88±1.30 μm, n=36) was significantly further from soma than that in control group (13.31±1.81 μm, n=18), *: P<0.05. Middle, Nav1.2 length in 20 mmol/L glucose-treated group (23.97±1.61 μm, n=36) was similar to that in control group (22.61±1.98 μm, n=18), ns: P>0.05. Right, distal end of Nav1.2 in 20 mmol/L glucose-treated group (42.85±2.08 μm, n=36) was similar to that in control group (35.92±2.21 μm, n=18), *: P<0.05.

C. Schematic of AnkG and Nav1.2 position in dendritic AISs in rats. AnkG, pink filled box, Nav1.2, green filled box.

D. In dendritic AIS neurons in mice, compared with control group (gray), AIS was slightly distally located in 3 h 20 mmol/L glucose-treated group (pink), while AIS length was similar. Left, proximal end of AIS in 20 mmol/L glucose-treated group (33.22±2.77 μm, n=29) was more distally located than that in control group (25.72±1.41 μm, n=24), *: P<0.05. Middle, AIS length in 20 mmol/L glucose-treated group (30.25±1.72 μm, n=29) was similar to that in control group (33.05±1.57 μm, n=24), ns: P>0.05. Right, distal end of AIS in 20 mmol/L glucose-treated group (63.47±3.12 μm, n=29) was similar to that in control group (58.77±1.91 μm, n=24), ns: P>0.05.

E. In dendritic AIS neurons in mice, compared with control group (gray), both Nav1.2 location and length were similar to 3 h 20 mmol/L glucose-treated group (pink). Left, proximal end of Nav1.2 in 20 mmol/L glucose-treated group (25.03±1.61 μm, n=20) was similar to that in control group (28.17±1.60 μm, n=18), ns: P>0.05. Middle, Nav1.2 length in 20 mmol/L glucose-treated group (33.11±2.42 μm, n=20) was similar to that in control group (27.96±1.79 μm, n=18), ns: P>0.05. Right, distal end of Nav1.2 in 20 mmol/L glucose-treated group (58.14±3.12 μm, n=20) was similar to that in control group (56.13±2.38 μm, n=18), ns: P>0.05.

F. Schematic of AnkG and Nav1.2 position in dendritic AISs in mice. AnkG, pink box, Nav1.2, green box.

Error bars represent SEM; two-tailed unpaired t-test was employed in A-B and D-E.

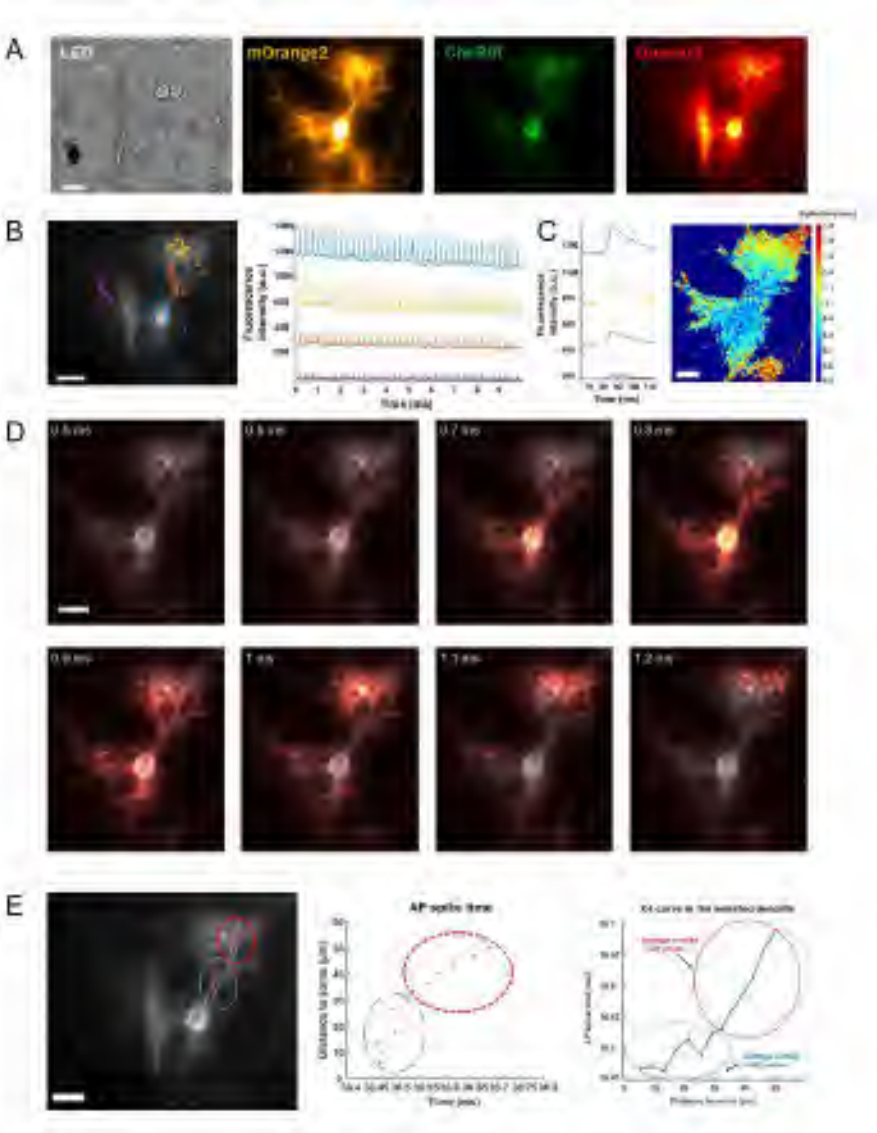

Supplementary Figure S4 Changes in velocity of AP propagation in dendrites were resolved well using voltage imaging

A. CheRiff-P2A-QuasAr2-mOrange2 (Optopatch2) (Hochbaum et al., 2014) was expressed in neurons to monitor AP propagation in dendrites. Panels from left to right show bright field image and fluorescence channels of mOrange2, CheRiff-EGPF, and QuasAr2, respectively. Scale bar: 20 μm.

B. Synchronized voltage imaging in simulated neuron with optogenetics. Left panel, ROIs selected in neurons are highlighted with different colors: blue: soma; orange, yellow, and purple: three ROIs in different dendrites adjacent to soma. Right panel, synchronized voltage imaging data from four ROIs corresponding to optogenetic stimulation (highlighted with light blue lines on top, 0.05 W/cm^2). Data were acquired at 464 Hz.

C. AP propagation was resolved well after upsampling. Left panel, 1 000 times upsampling average optical signal (interval=2 μs) in four ROIs was calculated by averaging multiple AP spikes shown in (b) with the same processing pathway described in Fig. 1. Here,

fluorescence intensity of the four ROIs was normalized. Right panel, AP propagation map showing clear propagation pattern from soma to dendrites.

D. Snapshots of average AP movies after upsampling processing; interval of four images is 0.1 ms (red represents arrival of AP on pixels).

E. AP propagation in a single dendrite. Left panel, selected dendrites in fluorescence image (QuasAr2 channel) are highlighted in white, and centerline of dendrite is labeled with red asterisks; middle panel, distance-to-soma AP spike timing plot at selected dendrites. Note, AP spike timings at different spatial acquisition units (red asterisks) reside in a time duration of less than one raw frame (2.1535 ms), and average "pitch" between different spatial acquisition units in these dendrites is approximately 3.7 μm. Right panel, x-t curve of selected dendrites. Red dots are the same as red asterisks in the other two columns, and solid blue line represents x-t relationship after smoothing. Clear non-uniform (deceleration) propagation from soma to distal dendrite is observed on the curve, highlighted by blue and red dashed circles.

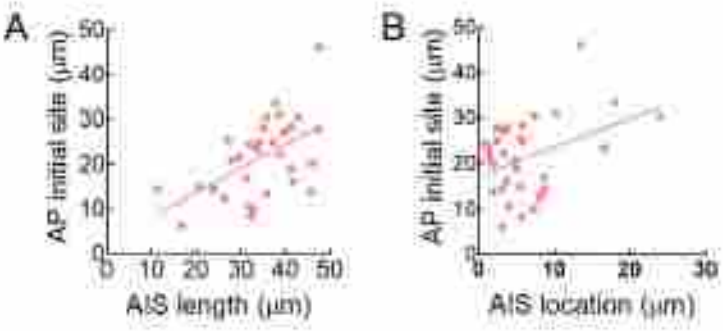

Supplementary Figure S5 APs were initiated more distally in longer/distally located AISs.

A. Correlation of AIS length and AP initiation site (n=32, r=0.5372, **: P<0.01).

B. Correlation of AIS location and AP initiation site (n=32, r=0.3820, *: P<0.05).

Supplementary Table S1. Spectral properties and filter sets of stains and fluorescent proteins used in this study.

Fluorophore	Excitation max. (nm)	Emission max. (nm)	Laser excitation wavelength (nm)	Emission filter (nm)
DAPI	350	470	405	460/50
Alexa Fluor® 405	401	421	405	460/50
Alexa Fluor® 488	490	525	488	525/50
mOrange2 (Shaner et al., 2008)	549	565	532	585/65
Alexa Fluor® 568	578	603	561	600/37
QuasAr2 (Hochbaum et al., 2014)	590	715	637	700/75
Alexa Fluor® 647	650	665	637	700/75

Dichroic mirror: Chroma ZT405/488/561/640rpc and ZT405/488/532/642rpc

Supplementary Table S2. Model parameters in Figure 4D-J

Compartment	Diameter × length ($\mu m \times \mu m$ μm × μm)	G_{Na} ($pS/\mu m^2$ pS/μm^2)	G_K ($pS/\mu m^2$ $pS/\mu m^2$)
dendrite	2×1000	100	20
soma	20×40	100	20
dendrite2	1.5 (0.8~2) ×1000	100	20
AIS	1.2 (0.8~2) ×40 (20~80)	5000	1000
axon	1.2 (0.6~2) ×1000	300	150

General parameters: C_m (specific membrane capacitance): 0.5 μF/cm^2; R_m (specific membrane resistance): 10000 Ω·cm^2; R_a (intracellular resistivity): 300 Ω·cm; E_L (leak reversal potential): -65 mV

Supplementary Table S3. Model parameters in Figure 5E and F

Compartment	diameter×length ($\mu m \times \mu m \mu m \times \mu m$)	G_{Na} ($pS/\mu m^2 pS/\mu m^2$)	G_K ($pS/\mu m^2$ pS/μm^2)
left cable	20×500	1200	360
(somatic)	2×50	1200	360
middle cable (dendritic)	3×50	1200	360
middle cable right cable	20×450	1200	360

General parameters: C_m (specific membrane capacitance): 1.0 μF/cm^2; R_m (specific membrane resistance): 1000 Ω·cm^2; R_a (intracellular resistivity): 100 Ω·cm; E_L (leak reversal potential): -65 mV